Morphological Studies of Nanowire Surfaces Using Scanning Probe Techniques

Johan V. Knutsson

Division of Synchrotron Radiation Research

Department of Physics

Lund University

Sweden

6/10/2012

LUND UNIVERSITY

Morphological Studies of Nanowire Surfaces Using Scanning Probe Techniques

Johan V. Knutsson

Johan.knutsson@gmail.com

A Master Thesis equivalent to 60 credits

Division of Synchrotron Radiation Research

Department of Physics

Supervisors:

Prof. Anders Mikkelsen

PhD-student Martin Hjort

June 18, 2012

LUND
UNIVERSITY

Abstract

Highly structured polytypic InAs III-V semiconductor nanowires with an axial stacking of *wurtzite* (WZ) and *zincblende* (ZB) segments were studied using scanning tunneling microscopy and spectroscopy (STM/S). The periodic changes in the axial direction of the crystal structure were achieved by precisely tuning the growth parameters, and no unwanted doping gradient was required. All low index facets of the wires were identified and characterized by atomically resolved STM images, revealing $\{10\bar{1}0\}$ and $\{11\bar{2}0\}$ terminations on the WZ facets, and $\{111\}$A/B as well as $\{110\}$ termination for the facets of the ZB crystal. In addition, the interfaces between these facets, of which some exhibited rotations, were also studied. The overall morphology of the wire as well as the morphology of the individual facets were determined, resulting in the creation of a model of the wire. The model includes conclusions regarding the origin of the surface morphology, and the implications such surface configurations might infer to the electronic properties as well as extended growth of such wires.

Preface

Acknowledgements

I would like to extent my sincere thanks to my supervisors Anders Mikkelsen and Martin Hjort for their genuine support and help during this project. In particular I would like to express my appreciation for the many rewarding discussions and the amount of jokes, with varying quality, that followed those. Additionally I would like to thank them both for letting me loose in the lab, spending endless hours scanning on crap in the belief of it being nanowires. However, ultimately those hours were fruitful since some nanowires were actually found.

Furthermore, I would like to thank everyone at the department, with special thanks extended to Olof Persson, Reiner Timm, Jalil Shahand, Anderas Johansson and last but not least Stephan Pröller, for keeping me company down in the lab. Additional gratitude is directed towards Niclas Johansson for the lunch dates at the Sausage house, boasting to have 101 different sausages.

Although totally unrelated, I would like to use this opportunity to express my gratitude towards Anna Stenvall, my love in life, for her unstinting laundry work.

On a more serious note I would like to express my thanks and appreciation towards Sebastian Lehmann for letting my study the wires that he so meticulously grew.

I would also like to extend my thankfulness towards the carpenters who renovated my designated office space. Without your, what must be thorough and methodical work, I would never have had the chance to appreciate the benefits of working from home for extended time periods.

Moreover, a project this size requires a certain amount of cinnamon buns as well as moral support, both of which my family so affectionately provided.

A last note of gratitude and thankfulness is directed towards my aunt, for without her I would never have had the possibility to start, and just as importantly, complete my studies. Thank you.

If it so happens to be that I have forgot to thank someone that I should have, I thank you for your forgiveness.

Johan V. Knutsson

Nanotrådar- små, men med stora möjligheter

Nanovetenskap anses ofta vara vägen till framtidens teknologi inom bland annat elektronik. Även om endast en liten del av fysikens alla aspekter är involverade inom området så finns det likväl en myriad av olika forskningsområden som alla kan klassas som nanoteknologi. Exempel på dessa är katalysatorer, kvantprickar men även belysning i from av LED.

En annan undergrupp, som studeras ingående vid Lunds Universitet är halvledande nanotrådar. En nanotråd är i princip en stavformad kristall vars diameter ofta mäts i tiotal nanometer och vars längd kan sträcka sig upp till flera mikrometer. Dessa nanotrådar, speciellt de som är gjorda av III-V material, dvs av en blandning av atomer från grupp III och grupp V i det periodiska systemet, har påvisat stor potential inom såväl elektronik som fotonik.

För att uppnå målet att använda dessa komponenter i framtidens elektronik måste först morfologin av ytorna samt skiften mellan olika kristallstruktur i trådarna studeras i detalj. Detta då förhållandet mellan atomerna på ytan och atomerna i bulken, d.v.s. inuti tråden, är väldigt stor på de små längdskalor relaterade med nanotrådar, till skillnad från motsvarande ratios för komponenter i dagens elektronik. Således kommer ytans egenskaper vilka beror på dess morfologi och atomstruktur, som i dagens elektronik till stor del är försumbara, att spela stor roll gällande trådarnas möjlighet att dominera i framtidens elektronik.

Ett optimalt redskap för sådana studier är ett så kallat *sveptunnelmikroskop* (STM) som, baserat på den kvantmekaniska tunneleffekten, kan uppnå upplösningar höga nog att se enskilda atomer. Denna typ av mikroskopi är dock oftast limiterade till extremt platta ytor, med maximala höjdskillnader på ett fåtal nanometer. Det är således en väldigt opraktiskt metod rent experimentellt för studier av nanotrådar, detta då höjdskillnaden mellan substrat och nanotråd är ofantligt stora i ett STM´s mått mätt. Detta har lett till att endast ett par studier av nanotrådars ytor har gjorts med hjälp av STM, vilket gör vikten av vidare studier ännu större.

Således inleddes en helomfattande STM studie av halvledande nanotrådars ytor med målet att övervinna de experimentella barriärerna vars resultat sammanfattas den här mastersavhandlingen. De studerade trådarna, bestående av InAs, var i sig speciella då de var multistrukturella, d.v.s. hade många olika facetter och atomära strukturer i en och samma tråd, varav somliga, kallade *Wurtzite*, en atomär struktur som för InAs endast observerats i naontrådar. Detta möjliggjorde direkta jämförelser mellan strukturerna på trådarna, och gav även möjligheten att i detalj studera övergångarna från en struktur till en annan. Dessa övergångar är av stort intresse då de förutspås kunna påverka de eftersökta elektroniska egenskaperna hos trådarna.

Handledare: Prof. **Anders Mikkelsen** och PhD-student **Martin Hjort**
Examensarbete 60 hp i fysik 2012
Fysiska institutionen, Avdelningen för synkrotronljusfysik, Lunds universitet

Project Introduction

The field of nanotechnology is generally considered to have the potential of revolutionizing our daily lives in the form of technological advancements. Although being a small field in itself, it consists of many subgroups as for instance catalytic research and quantum dot electronics. One other major sub field, which is widely explored at Lund University, is that of semiconducting nanowires. A nanowire is essentially a rod shaped crystal with typical diameters in the order of ten nanometers (nm) and lengths up to several micrometers (μm).

Such semiconducting nano devices, and especially III-V heterostructure nanowires, consisting of atoms from both group III and V in the periodic table, exhibit great potential for multipurpose use within the field of electronics and photonics [**1**–**3**].The applicability of such wires is however highly dependent on crystal structure as well as defect density [**4**] and general surface morphology [**5**], since such factors can have great impacts on electronic properties [**1**, **6**]. However, the extent of direct studies of nanowire surfaces is very limited due to experimental limitations related to in depth nanostructure imaging, and only a few publications regarding direct atomic scale imaging have been published [**7**–**9**]. The mentioned properties would however ideally be studied with an STM due to its ability to assess the atomic structure and morphology in addition to probing the electronic properties of the nanowire surface. Additionally, regarding III-V materials, some atomic structures such as the wurtzite structure have only been seen in nanowires and thought to be non-existent in bulk form [**2**, **10**]. Hence in order to fully comprehend the properties and potential of such rare crystal formations, STM studies are vital.

One limiting factor regarding nanowire STM studies is the inability to quickly find and evaluate new samples. In addition, the severe dependence on tip quality might render the data of electronic properties between two sets of wires incomparable if major tip changes occurred [**11**]. However, by precisely tuning the growth parameters, the crystal engineered InAs nanowires studied in this thesis could be created, exhibiting both Wurtzite (WZ) and Zincblende (ZB) segments with a periodicity and segment length predetermined by the growth parameters [**2**, **6**, **10**, **12**]. Experimentally such wires are perfect for STM studies since the two atomic structures can be investigated in a single image as long as an interface can be found. An additional topic of interest is the investigation of potential overgrowth of certain facets since it can have a significant effect on nanowire device performance.

Additionally, the interfaces themselves deserve a certain amount of attention since changes in electronic properties as well as stacking fault density are thought to be increased in such areas [**6**]. More so is the superlattice twinning (TSL) mirrored facets with different termination, which often occurs during ZB growth since it can induce direct band gaps in otherwise indirect materials [**12**]. As a result of the multifaceting, some interfaces are expected to be rotated with respect to each other, and naturally scanning on such interfaces poses a great challenge.

Hence, the STM and STS studies conducted in this thesis, investigating and characterizing the various surface facets of such wires might prove valuable when regarding further understanding of nanowire growth and potential future applications within the field.

Contents

Abstract iii

Preface v
Acknowledgements v
Populäravetenskaplig Sammanfattning vii
Project Introduction ix

Part 1. Introduction 1

Chapter 1. Semiconductors 3

Chapter 2. Surfaces and Crystals 5
1. Crystallographic directions 5
2. Nanowire surfaces and structure 6
3. Surface reconstructions 9

Chapter 3. Experimental Methods 11
1. Scanning Tunneling Microscopy, STM 11
2. Scanning Tunneling Spectroscopy, STS 15
3. Scanning Electron Microscopy, SEM 18

Chapter 4. Nanowires 21
1. Nanowire growth 21

Chapter 5. Sample preparation 25
1. Nanowire transfer 25
2. Deoxidation 25

Part 2. Experiments and Results 27

Chapter 6. Crystal Engineered InAs Nanowires 29
1. Experimental 29
2. Results 30

Chapter 7. Summary 57

Outlook 59

Appendix. Bibliography 63

Part 1

Introduction

CHAPTER 1

Semiconductors

Semiconductors, intrinsically having an electrical conductivity in the regime in between a true conductor and insulator, are often referred to as the foundation of modern electronics. The success of semiconductors is however closely related to their ability to act as both a conductor and an insulator given certain conditions. By for instance introducing low concentrations of well-chosen impurities into the semiconductor crystal, called dopants, additional states within the bandgap can be induced which in turn alters the conductive properties of the crystal. Hence, by utilizing different dopants, i.e. donors and acceptors, a basic transistor can be created, having a high respectively low conductivity depending on the polarity of the applied voltage. Other devices such as high performance solar cells and LEDs can be created similarly.

Traditionally, silicon has been used commercially due to low production costs and high availability. In recent years however compound materials, usually from group III and V of the periodic table, have been introduced. Such materials, often referred to as III-V semiconductors, have the advantage of a direct band gap, higher charge mobility in addition to the ability to covering a wider band gap range [**13**]. High production costs related to problems regarding integration with existing manufacturing techniques of the well-researched silicon semiconductors, in addition to unstable oxide formation and lattice mismatches are one of the main reasons to the limited use of III-V materials commercially.

Regardless, the potency of III-V semiconductors may lead the way to the future of electronics given time and research. One route might very well be III-V materials in the form of nanowires, being crystalline structures shaped as rods in the nano regime. Many different III-V compounds have been fabricated in the form of nanowires, but InAs, being the material mainly studied in this thesis, has one of the highest electron mobility of III-V semiconductors, making it a given candidate for future electronic applications [**14**].

CHAPTER 2

Surfaces and Crystals

When the surface to volume ratio reaches critical values, as is common for nanostructures, the electronic properties will be dominated by the surface rather than the bulk [**13**]. Hence, a fundamental understanding and characterization of crystalline surfaces is required when prospecting future applications of nano devices, such as for instance nanowires. A brief introduction is given below.

1. Crystallographic directions

The atomic arrangement in a perfect crystal is periodic in nature and can be considered as a three dimensional lattice. Mathematically, such a structure can be described by the smallest reoccurrence in the structure, represented by blocks of atoms often referred to as *unit cells*. The relative position of atoms within such a cell can be defined by a set of *base vectors*.

Several lattice configurations are possible depending on the relative orientation of the base vectors. Put under a collective name, all such configurations are referred to as *Bravais lattices*. A Bravais lattice defines the relative orientation of all possible lattice points in a crystal structure, and thus delimits how each individual atomic layer is constructed as well as the sequential stacking of the crystal.

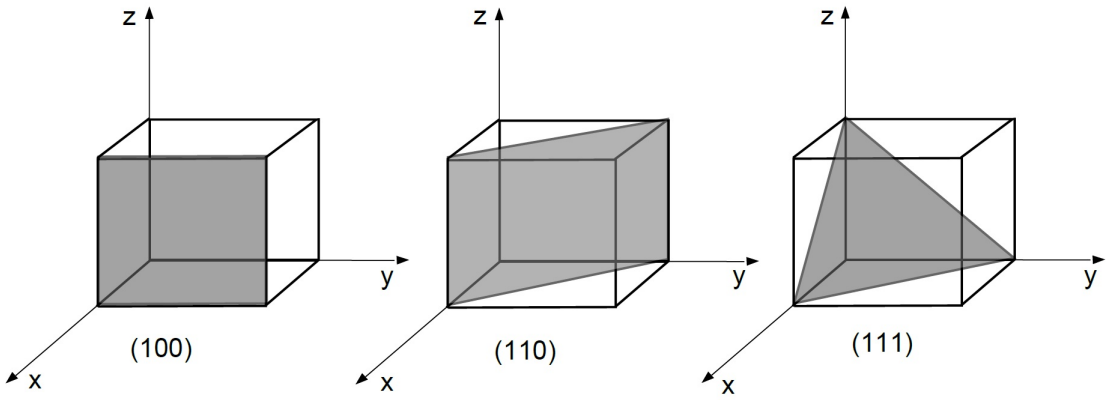

FIGURE 2.1. Three common *low-index* planes for cubic lattice structures.

All possible atomic structures of a crystal surface can be defined by cutting the Bravais lattice of the crystal in different planes. The planes, and their respective lattice points, are defined by the three points where the plane intercepts the x, y and z-axis. The distance from the origin, (000), to the interception points is measured in units of the lattice constant a, defined as the distance between two lattice points. Thus one can use the indexes (hkl), known

as *Miller indices*, as a notation for a specific plane. However, when regarding hexagonal structures, an additional dimension is required, and Miller indices for such crystals are denoted $(hkli)$. A demonstration of a few planes for a cubic lattice is given in fig. 2.1.

Depending on the unit cell of the crystal and the plane it is cut, the resulting facet will exhibit different atomic structures as demonstrated by fig. 2.2

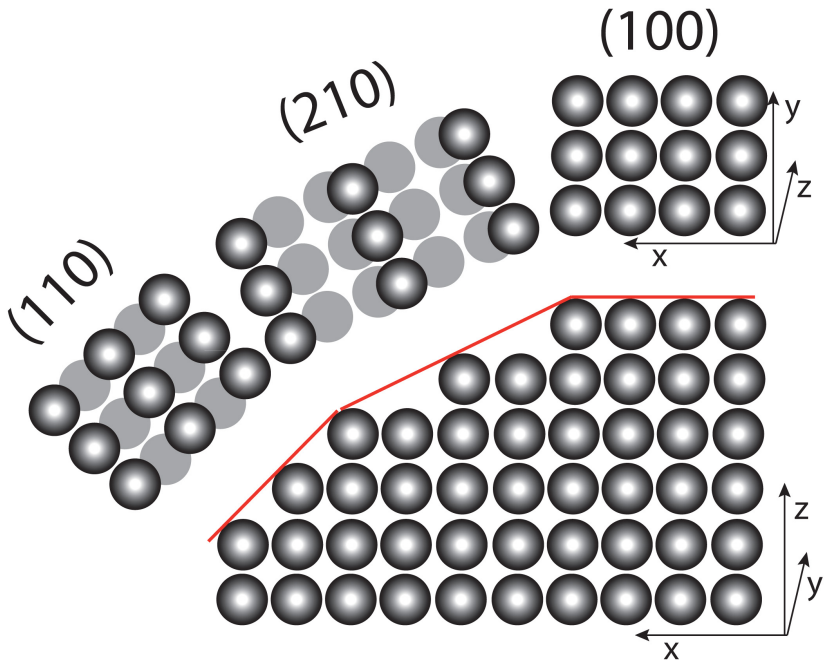

FIGURE 2.2. The image illustrates that depending on which plane a crystal is cut, the atomic pattern of the resulting surface will be different. The image assumes a monoatomic simple cubic crystal lattice. Image inspired by [**15**].

2. Nanowire surfaces and structure

The surface of the nanowire facets is of great importance due to the exceptionally large surface to volume ratio of such devices. At critical values, achieved for most nanowires, the given ratio will render the surface the dominating part regarding electronic or optical properties of the wire [**16**]. Hence, the morphology of nanowire surfaces must be mapped out and understood in order to be able to tailor specific properties of nanowires.

Additionally, due to the fact that some crystal formations of III-V materials, such as the hexagonal Wurtzite (WZ) structure, can be found only in nanowires [**10**], the importance of nanowire surfaces increases further. The most common resulting facets of WZ, assuming that it is grown in the (111)B direction, are the $\{10\bar{1}0\}$ and $\{11\bar{2}0\}$ planes. The mechanism of the formation of such WZ related surfaces is described in detail in [**10**].

Although nanowire studies with *transmission electron microscopy* (TEM) have been conducted, such experiments will only reveal the average atomic structure and stacking fault density. In order to study the actual morphology, including vacancies, adatoms, surface

reconstructions, steps and kinks, and its impact on the electronic properties, experiments utilizing STM in conjunction with STS must be conducted.

Another typical crystal structure of III-V nanowires, is the cubic Zincblende (ZB), most commonly presented in the form of {110} and {112} facets, again assuming growth in the (111)B direction [**1**, **2**].

Many III-V nanowires exhibit both ZB and WZ growth, being polytypic in nature, a phenomenon accompanied by a lot of investigation [**10**, **17**]. In a III-V nanowire, a single bilayer of the wire is defined as a pair of group III and a group V atom. The bilayer stacking for the cubic ZB is ABCABC, whereas it is ABAB for the hexagonal WZ, when viewed in the $\{\overline{1}\overline{1}\overline{1}\}$ and $\{000\overline{1}\}$ direction respectively. Due to the similarity between the two structures, a stacking fault in one of them will give rise to a single segment of the other structure. If for instance in a WZ crystal, a misplacement of a bilayer in the stacking sequence, denoted by the vertical bar, occurs, resulting in a AB<u>AB</u>|<u>C</u>BCB sequence, a segment of ZB (underlined) is formed [**6**].

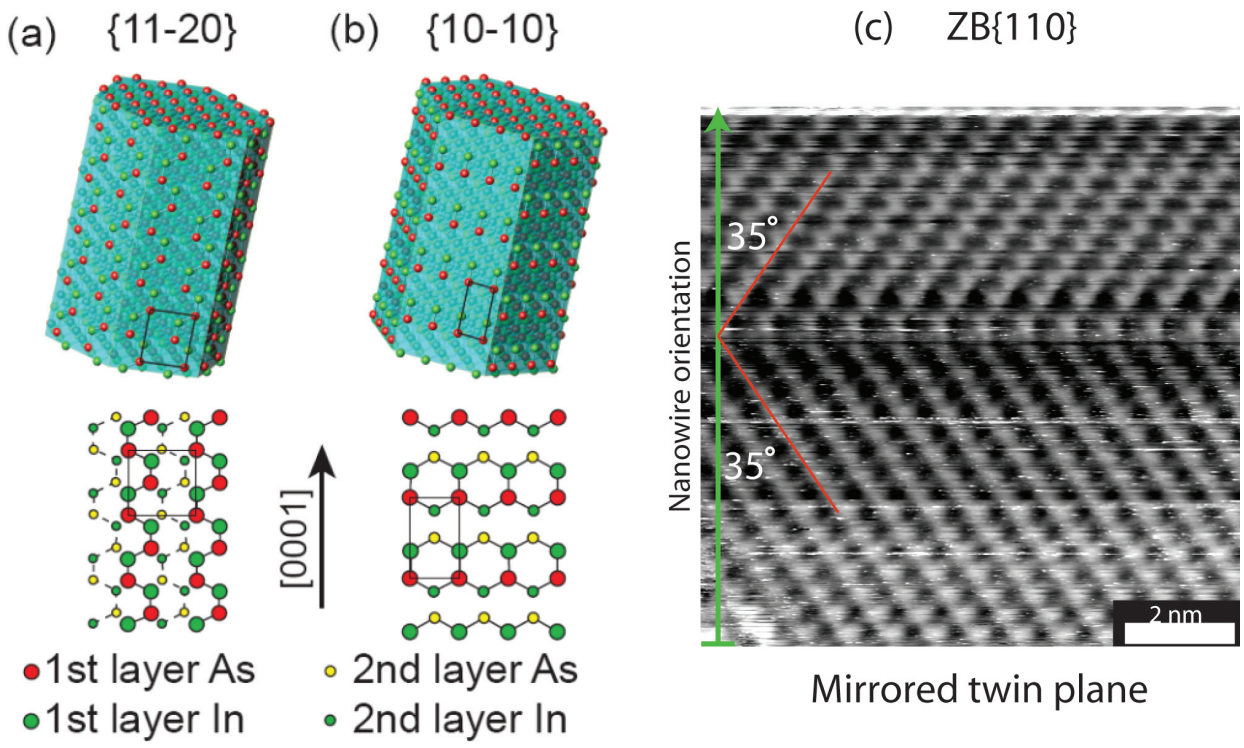

FIGURE 2.3. Figure (a) and (b) depicts a 3D model of the two most common planes of a WZ crystal, being $\{11\overline{2}0\}$ and $\{10\overline{1}0\}$ respectively. The bottom part of those figures displays the relative orientation of the atoms in the two uppermost layers of such a plane. Figure (c) depicts the interface between two mirrored {110} planes of a ZB crystal. The mirroring is a result of an underlying TSL structure, and is not normally found on ZB{110} surfaces. Figure (a) and (b) taken from [**17**].

However, a similar displacement of a bilayer of a ZB crystal occurs, ABC$\underline{\text{A}}$CBA, will not result in the formation of a WZ segment. Instead a twin plane, with an interface denoted $\underline{\text{A}}$, is formed, being a mirrored plane rotated 70°with respect to the original plane as depicted in fig. 2.3c.

In order for a WZ structure to form, two consecutive stacking faults, or twin planes, must occur in the ZB crystal AB$\underline{\text{CA}}|\underline{\text{C}}|\underline{\text{A}}$.

These different facets, of both WZ and ZB, all exhibit very different atomic structures, making them easy to identify in atomically resolved STM images. As for instance illustrated in fig. 2.3, the WZ facets $\{10\bar{1}0\}$ and $\{11\bar{2}0\}$ exhibit a zig-zag pattern and atomic rows perpendicular to the growth direction respectively. The atomic structure of ZB $\{110\}$ plane will exhibit rows with a 35°rotation with respect to the growth axis, i.e. (111) direction.

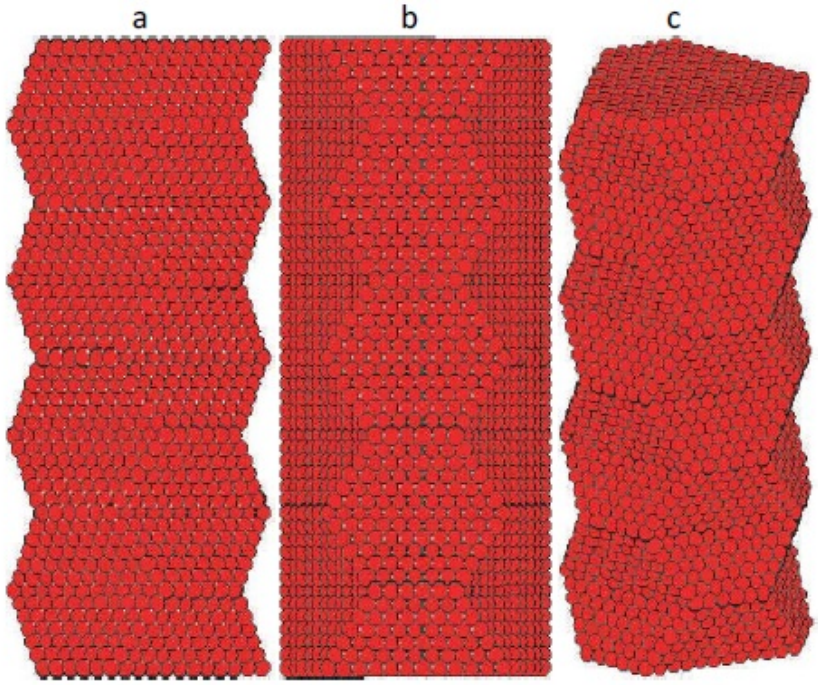

FIGURE 2.4. A model of the TSL structure, consisting of sequential octahedral segments, shown from different angles. Image taken from [**17**] (originally from [**18**]).

Another common structure seen in ZB nanowires is a multifaceted structure, known as *twinned super lattice* (TSL) if periodic, constructed of several sequential octahedral segments terminated by $\{111\}$ planes [**18**] as illustrated in fig. 2.4. Such structures are of interest since they for instance are predicted to give rise to direct band gaps in semiconductors that normally display indirect bandgaps [**12**]. It has also been noted that a TSL structure can give rise to minibands [**12**]. If, during growth, some parameters are tuned the TSL will be overgrown, resulting in the mentioned $\{110\}$ facets. These facets will be rotated with respect to the $\{111\}$ planes as seen in fig. 6.1 at page 30.

3. Surface reconstructions

In a bulk crystal, each atom is surrounded by neighboring atoms, satisfying the bonds of such atoms. However, when a crystal is cleaved the atoms exposed at the surface will have unsatisfied bonds, which is energetically unfavorable. Such surfaces will thus prefer to adsorb adatoms, or reconstruct to a new atomic structure, with lower potential energy, in order to satisfy the dangling bonds [**19**].

In some cases, the surface atoms will regroup and form dimers or trimers, being two respectively three atoms bound together. In the case of trimers, a triangular formation is common. When studied in STM, the individual atoms in a dimer or trimer can be hard to resolve, making them appear as very big atoms, with a possible triangular shape when regarding trimers. Thus, if studying a surface reconstruction, forming a lattice of trimers, in an STM, large triangular atoms with a suspiciously large interatomic distance would be seen.

CHAPTER 3

Experimental Methods

Several experimental methods were used in the investigations of nanowire surfaces involved in this thesis. The most important ones, *scanning tunneling microscopy* (STM), *scanning tunneling spectroscopy* (STS) and *scanning electron microscopy* (SEM), are described in detail in this chapter. In short, STM is a very local and nondestructive investigative method yielding highly resolved images of real space by measuring tunneling currents. Often used in connection with STM imaging is STS, a common and useful tool probing the electronic properties near the Fermi level of a material. The SEM is often used in order to obtain overview images of nanostructures as well as their abundance and position on the substrates.

1. Scanning Tunneling Microscopy, STM

The first successful experiments regarding the usage of vacuum as a tunneling barrier were done by G. Binnig *et al.* [**20**, **21**] in 1982. The success quickly lead the very same group to later that year invent and develop a novel surface imaging technique which came to be called *Scanning Tunneling Microscope* (STM) [**22**, **23**]. The ability of the STM to analyze topographic and electronic properties of conducting surfaces with atomic resolution in real space [**24**, **25**] forced many surface models to be revised [**26**, **27**] and have since then revolutionized the field of surface science and crystallography. Although the electronics and aperture have been developed a lot since its invention, the basic principle remains the same.

An atomically sharp metal tip, usually made out of Tungsten (W) or a Platinum/Iridium alloy (Pt)/(Ir) [**28**], is attached to a *piezodrive* and brought in close proximity of, and precisely scanned over, a conductive surface. Upon applying a small *tunneling voltage* V between tip and sample, a tunneling current I, typically in the order of pA-nA, will flow, provided that the tip-sample separation s is small enough, i.e. around 10 Å. Tersoff et. al. [**29**] showed that the tunneling current decreases exponentially with tip-sample separation in accordance to eq. 1,

$$I \propto e^{-2s\kappa}, \tag{1}$$

where κ denotes the current decay rate, implying that a very high vertical resolution can be achieved. The direction of the current is dependent on the polarity of the bias. By applying a positive bias to the tip, electrons will tunnel from the tip into the sample, meaning that empty electronic states are probed. If, on the other hand, a negative bias is applied, the electrons will tunnel from the sample to the tip, probing filled electronic states, see fig. 3.1 for further explanation.

By recording the current in discrete points, while the tip is raster scanned across the surface, a topographic image can be constructed. The exponential dependence ensures that only

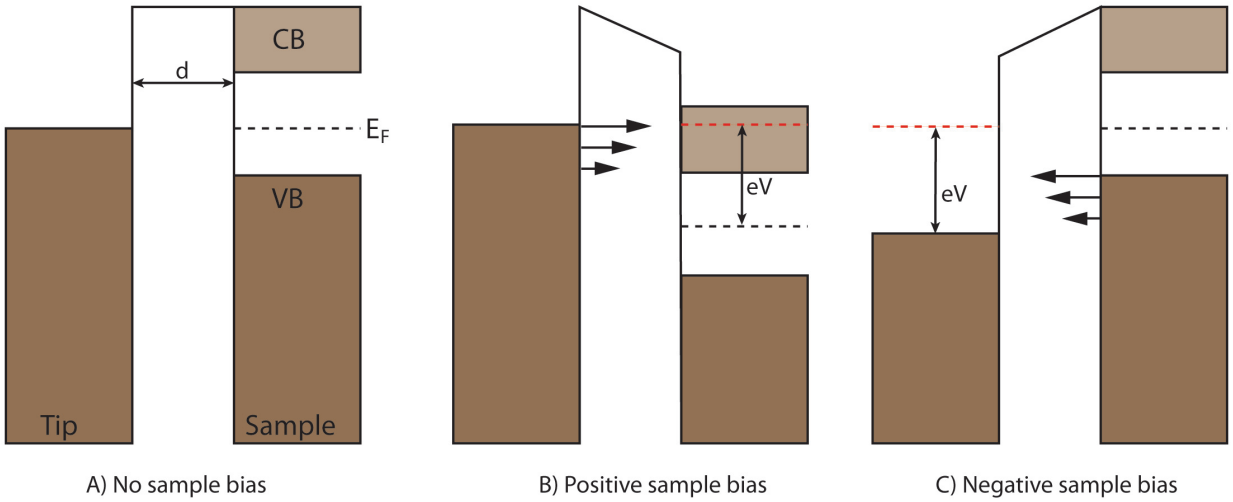

FIGURE 3.1. The figure illustrates how the tunneling is dependent on the magnitude as well as polarity of the applied bias voltage V. In figure A), no bias is applied and hence the tip and sample are in equilibrium, i.e. aligned Fermi levels E_F. In figure B), a positive sample bias is applied, causing electrons to flow from the filled states of the tip into the empty states in the conduction band (CB) of the sample. In analogy, when a negative bias is applied, as demonstrated in figure C), electrons will flow from filled states in the valence band (VB) of the sample into empty states of the tip. As indicated in the figures, only electronic states within eV will contribute to the tunneling.

the closest atom is imaged. This also infers a very high lateral resolution of the constructed image. The process is illustrated in fig. 3.2.

The scanning process can be done in a couple of ways. In the so called *constant current mode* the current is set to a fixed value and kept constant during scanning by moving the tip up or down using the piezo elements. The resulting movement of the tip represents a contour of the sample surface. The vertical displacement of the tip is recorded as a function of sample position and can be translated into an image. The other possibility is to use the *constant height mode*, in which the vertical position of the tip is constant, and the image is constructed directly from the changes in the tunneling current. The latter method has the advantage of improved scan speed, since the tip does not change its vertical position. The method however requires very flat surfaces, i.e. on the scale of a few nm, in order not to crash in to something, making it unsuitable for nanostructure imaging which usually involves heights of tens of nm. Hence, only the constant current mode was used during experiments involving nanowires.

Due to the small tip-sample separation during scanning, the success of STM imaging is highly dependent on vibrational isolation from both acoustic and mechanical sources [**30**]. Hence, it is essential that the STM system is placed on a table with built in dampening. In addition, the STM itself, i.e. the tip and sample, is often dampened by a combination of a spring system and a magnetic system. The purpose of the magnetic system is to greatly increase the dampening factor of any oscillation that would occur in the springs. The STM

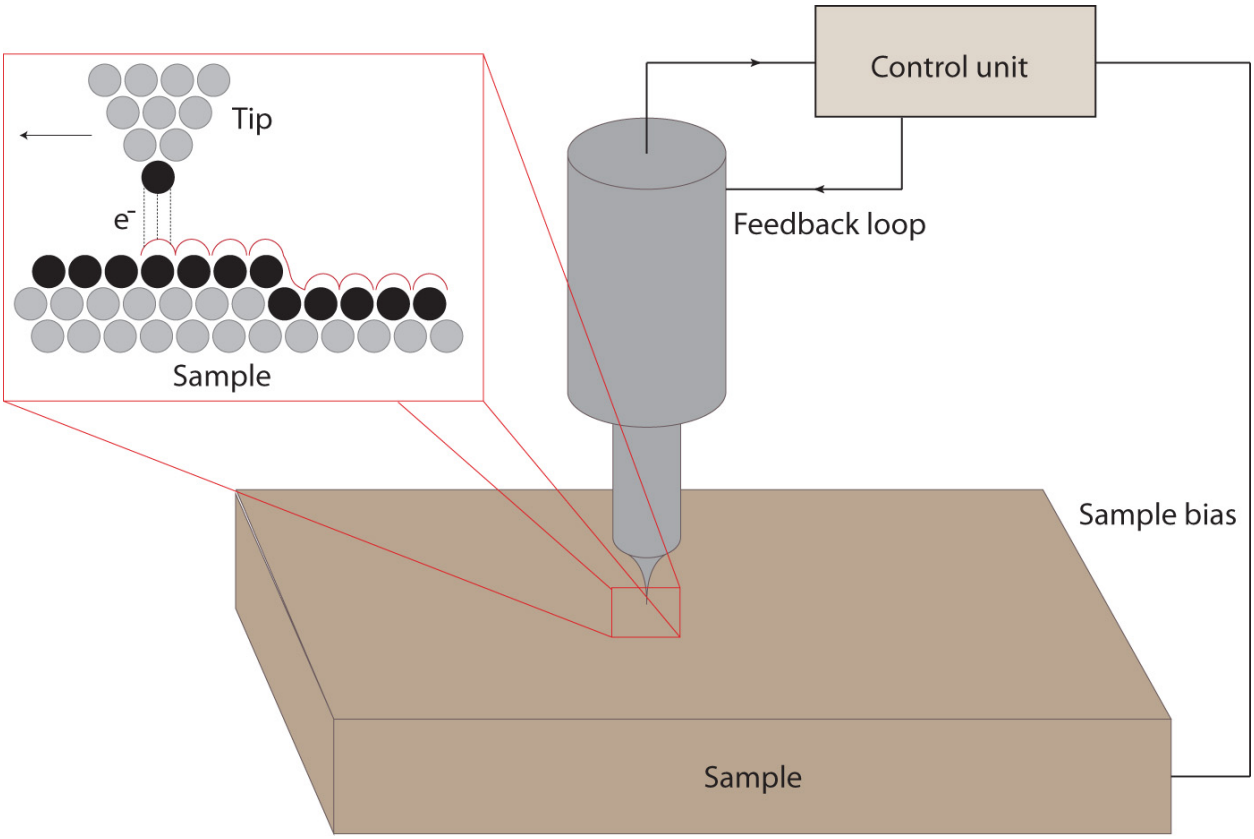

FIGURE 3.2. The image illustrates the scanning process of an STM. The tip is scanned along the surface at an appropriate tip-sample distance, small enough for tunneling to occur. In the inset figure, the region between the tip and sample is enlarged. The black atoms represent those of the atoms that are involved in the tunneling process. The red curve represents the resulting line profile, due to the measured tunneling current, of the scan. The region involved in electron tunneling is indicated by the dashed lines.

used for this thesis, a commercial Omicron XA STM, utilizes the above mentioned suspension system.

Although an STM can operate in conditions less strict than UHV, the samples studied will degrade rapidly if not introduced to such an environment, i.e. pressures in the order of $1 \cdot 10^{-10}$ mbar. The above mentioned Omicron XA STM was operated at room temperature, and all imaging experiments were done at a base pressure of $< 1 \cdot 10^{-11}$ mbar.

The prerequisites of the tip sharpness put a lot of demands on the tip production and preparation. The most common technique of producing an atomically sharp tip is by electrochemical etching, a method described in detail in [**31**–**33**]. The tips used for the experiments related to this thesis were all made in-house using the mentioned method. After introduction to the vacuum of the STM system, they were ridded by oxides by sputtering with Ar ions, a process that in addition often results in a slight sharpening of the tip.

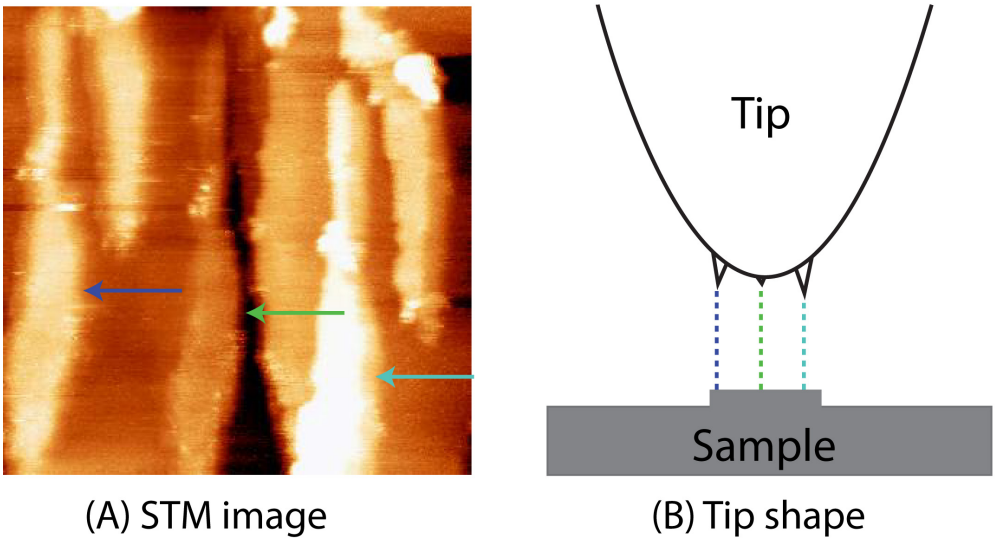

FIGURE 3.3. The STM image in (A) exhibits double (triple) features, as a result of a double tip which is schematically illustrated in (B). The triple features are marked out with arrows.

1.1. Artifacts and Image Interpretation. One of the downsides with STM is the many artifacts that can occur during scanning. They often originate in the fact that the surface is never directly observed, only the electronic density of states at the surface. Hence, a certain amount of thoughtfulness and understanding is necessity when interpreting STM data.

The theory of STM [**29**] assumes a symmetrical tip, with a single atom at its apex, and images are constructed in accordance to that model. In reality however, the tip might not always be symmetric. Hence, the shape of the tip greatly influences the appearance of the created image. On the atomic scale this would give rise to an elongation of the corrugation maxima in a direction related to the tip asymmetry [**34**]. On the larger scale, objects might appear bigger with distorted shapes.

In addition, multiple tips might have formed, giving rise to so called *double features* [**33**]. Due to the presence of multiple tips an image is formed which is a convolution between the images of all the tips. In such an image certain features might appear several times at different positions in the image as illustrated in fig. 3.3. The distance between the mirrored features corresponds to the real space distance between the different tips.

Thermic drift as well as creep in the piezo electric elements might result in distorted images, being smeared out in one direction as if the substrate was moving. This can be circumvented by abstaining scanning directly after large movements with the piezo or directly after sample heating.

Not as dependent on the tip shape, but more so one the principles of the imaging process itself is the fact that the atomic scale corrugation of semiconductor surfaces is mostly dominated by electronic effects, and not, as for most metallic surfaces, by the actual surface

corrugation [**34**]. This can be understood when considering that the tunneling current arises from the overlap of the local electronic states of the tip and sample, hence the contrast in such an image should be interpreted as the convolution of the density of those states [**24**]. For metallic samples, the STM image will have a close correlation to the topography of the surface since the local density of states is rather constant with respect to energy, i.e. tunneling voltage. For semiconductors however, the very same quantity varies strongly, especially at the band edges, resulting in a much harder interpretation when imaging such surfaces [**28**]. It was for instance showed by R. M. Feenstra et. al. [**35**], when studying a GaAs(110) surface, that there was a difference in lateral position of the local state maxima for the occupied and unoccupied band edge states. Hence, depending on the polarity of the voltage, the atoms appeared in different positions, being the Gallium (Ga) atoms for positive biases and Arsenic (As) for negative. A detailed description to this phenomenon is given in [**36**]. This implies that extra care has to be taken when analysing STM images of semiconductor surfaces.

An artifact only related to nanowire imaging is that the wires often appear to be significantly broader than expected. The thickness of a nanowire is often small with respect to the sharpness of the probing tip. The resulting image, being a convolution of tip and wire, would thus be a broadened nanowire. In an sense the quality and symmetry of the tip can be roughly estimated by scanning over a well-defined nanostructure such as a nanowire.

1.2. Imaging Nanostructures. Scanning on surfaces being sporadically covered with nanostructures, such as nanowires, give rise to a number of problems. Firstly, the sample of interest must be found, a process which is both problematic and time consuming. Fortunately, nanowires can often be seen optically by using a powerful CCD camera, making locating their general area easy. The real problem is to find a single wire within this area. A very low scan speed in conjunction with a high loop gain must be used since the nanowires are, from an STM point of view, very high, meaning that the tip is very likely to crash in to such obstacles when scanning. The drawback of a high loopgain is that it in effect makes the system more sensitive to vibrations, and effectively lowers the resolution by increasing the noise. However, when a wire is located the loopgain and scan speed can be changed to common values for surface imaging.

It does happen that nanostructures get picked up by the tip causing severe problems when scanning. This is often solved by applying a voltage pulse in the range of 4-10V

2. Scanning Tunneling Spectroscopy, STS

The inventors of the STM, Binning *et al.*, were also the first to realize the correlation between applied scanning voltage and surface topography [**37**]. Depending on the polarity of the bias, the atomic structure of a Si(111)-(7x7) surface differed. This was explained by tunneling through certain discrete states of the surface, only available at certain biases. This discovery is the very foundation of *scanning tunneling spectroscopy* (STS), a now vital complementary tool to STM. Although voltage dependent imaging yields a rough estimate of electronic structure, it can be further investigated by scanning over the whole bias range in a single, well chosen, point of interest.

A basic STS-spectrum is achieved by disengaging the feedback loop, keeping the tip-sample separation as well as tip position constant, and sweeping the applied voltage between

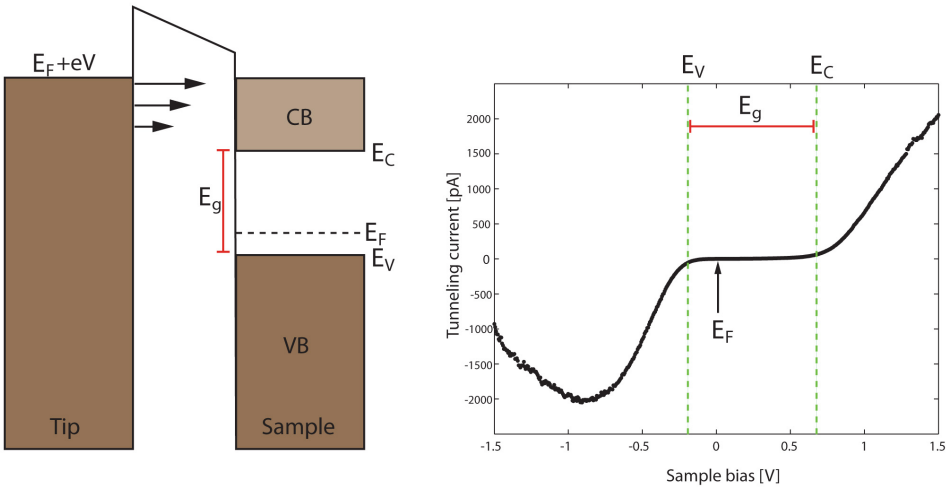

FIGURE 3.4. The figure illustrates the tunneling process when a voltage V is applied between tip and sample. States between E_F+eV (tip) and E_F (sample) contribute to the tunneling current. By continuously varying the applied bias an I/V spectrum (left) can be obtained yielding information regarding for instance Fermi level location within the bandgap (E_F), band gap width (E_g), as well as valence and conduction band onsets/offsets (E_V and E_C). The decrease in current between -1.5 and -1.0 V is related to the usage of variable z mode, which is explained in the section below.

two set values. The exponential relation of wave function coupling between tip and sample with respect to their relative real space distance ensures a high lateral precision. If done during STM scanning, which is conventional, the imaging process is temporarily halted.

In analogy to STM, STS theory necessitates that when a scanning bias V is applied, only states between the Fermi level E_F and $E_F + eV$, where e represents the elementary charge, contribute to the tunneling current [**11**]. Hence, by continuously varying the applied bias, and record the corresponding current, different states of the surface will consequently be probed, resulting in an s-shaped I/V spectrum. The magnitude of the measured current, at a given applied bias giving vital information regarding the electronic structure of the surface in the energetic vicinity of the Fermi level [**28**], i.e. a few eV. Interestingly, surface states in semiconductors, i.e. from dangling bonds, can often be found within the given energy range [**34**] rendering STS invaluable when investigating such states. Such, as well as other, states will be revealed in an I/V-spectrum as small bumps and kinks around the Fermi level.

A typical I/V-spectrum, obtained on an n-doped InAs(111)B semiconductor surface, is displayed in fig. 3.4. In the figure, key sites such as the Fermi level E_F, band gap E_g as well as valence and conduction band offsets/onsets, E_V and E_C respectively, are mapped out. Depending on doping parameters, and their ability to change the Fermi level position [**38**], the curve would effectively be shifted towards negative biases when being heavily n-doped and towards positive biases when p-doped.

However, the current signal at low applied voltages, i.e. close to the Fermi level, for such a spectrum will be significantly lower than for higher values, due to the exponential dependence given by eq. 1, effectively drowning the signal at low voltages. Hence, wanted

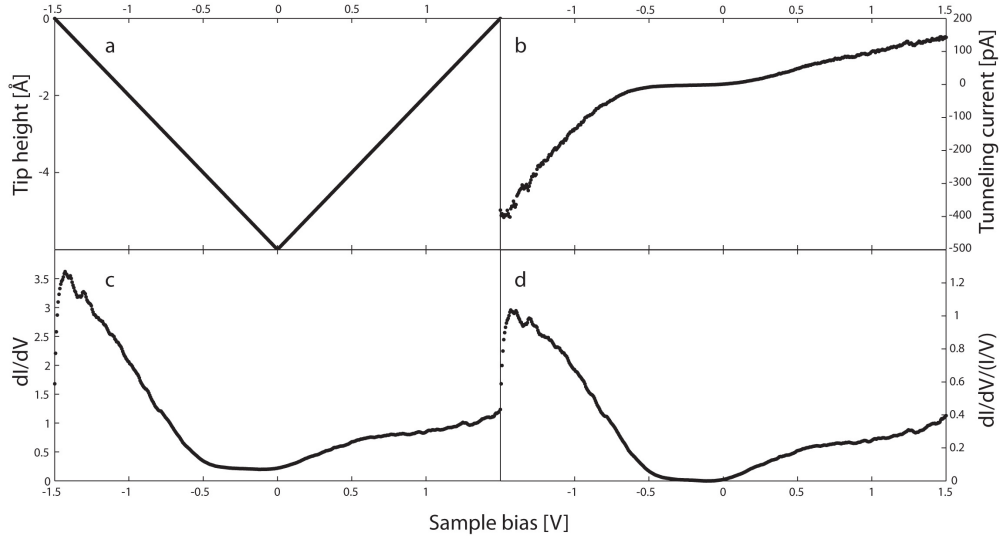

FIGURE 3.5. The figure shows the STS data at different stages in the data treatment process related to variable z mode. In (a), the tip height is given as a function of the applied bias. Figure (b) represents the obtained I/V spectrum. In (c), the differential dI/dV spectrum can be seen. The final normalized $(\frac{dI}{dV})/(\overline{I/V})$ spectrum is given in (d). Image inspired by [**17**].

details such as surface states will be obscured. This is solved by a utilizing the variable z mode described below [**34**].

2.1. Feenstra Mode. Additional problems arise when considering semiconductor surfaces due to the very low *local density of states* (LDOS) within the band gap. In such an area, only a negligible tunneling current can be measured, imposing certain modification to the acquisition technique regarding semiconductors if detailed spectroscopic data is to be extracted. P. Mårtensson and R.M. Feenstra suggested in 1989 [**39**] that the current signal could be significantly increased by varying the tip-sample separation as a function of the applied voltage, $\Delta s(V)$. A continuous linear function was used, see eq. 2, where s_0 represents the original tip-sample separation and a, the displacement factor. This solution, by varying the tip position in the z direction, is commonly called *Feenstra mode* or simply the *variable z mode*.

$$\Delta s(V) = s_0 + a|V| \tag{2}$$

Naturally, certain alterations must be done regarding data analysis when utilizing the varying z mode since the changes in tip-sample separation must be accounted for. It has been shown [**40**] that this dependence effectively could be removed by normalizing the differential conductance (dI/dV) with total conductance (I/V), yielding: $(dI/dV)/(I/V)$, a ratio that is directly proportional to LDOS. This normalization can be validated if realizing that the measured current I_m can be expressed as the current as if recorded at a constant position I_s, as described in eq. 3.

$$I_m(V) = I_s(V)exp^{-2\kappa\Delta s(V)} \tag{3}$$

When differentiated, the following expression is obtained:

$$\left[\frac{dI}{dV}\right]_m = \left[\frac{dI}{dV}\right]_s exp^{-2\kappa\Delta s(V)} \tag{4}$$

As stated, the previously suggested normalization, between eq. 4 and 3, will remove the exponential dependence. Although this technique have proven to be solid regarding metals or small band gap materials, the ratio has an inclination towards diverging at the band edges for larger band gap materials such as semiconductors. This problem was efficiently worked around by broadening the total conductivity, usually denoted as $(\overline{I/V})$ [**39**]. The resulting $(\frac{dI}{dV})/(\overline{I/V})$ curve will give a proper and detailed representation of the local density of states for a set voltage span, with only negligible tip-sample dependence [**40**]. The process is illustrated in fig. 3.5.

The actual dI/dV signal is obtained by using a lock in technique and superimposing a small frequency modulation onto the applied voltage, making it possible to measure the small variations in the tunneling current.

2.2. Surface Effects. When studying nanostructures, the surface to volume ratio can reach a critical value where the properties of the surface rather then the bulk will be the determining factor regarding electronic properties [**16**]. Due to the reduced number of degrees of freedom for the surface atoms constituting a crystalline surface, they will exhibit a certain amount of dangling bonds. If the potential of those bonds is somewhat distorted, i.e. by surface steps or adsorbents, it might give rise to surface states positioned within the bandgap of a semiconductor material [**28**, **41**]. Such states are known to pin the Fermi level, i.e. screening the electronic properties of the bulk, resulting in an apparent Fermi level denoted only by the average energy of the surface states. Hence, in order to obtain a viable spectrum, free from screening effects, only flat and uncontaminated areas should be probed.

An additional effect that can perturb the electronic structure is *tip induced band bending* (TIBB). Essentially it arises since some of the potential difference between tip and sample is dropped within the semiconductor, giving rise an apparent shift in the band structure [**42**], as depicted in fig. 3.6. STS data is acquired on the basis that a probed state of energy E can be related to the applied voltage V, according to: $E = E_F + eV$, where E_F denotes the Fermi level. However, when taking TIBB into account this expression must be adjusted by a term ϕ, representing the band bending at the surface: $E = E_F + eV - \Phi$.

Since band offsets is of major interest when doing STS such effects poses a severe problem regarding the evaluation of experimental data. Fortunately, quantitative estimations of the band bending have successfully been done [**11**, **43**], still making STS a viable investigative tool regarding band offsets.

3. Scanning Electron Microscopy, SEM

Scanning electron microscopy (SEM) is a versatile method when considering investigations involving structures in the nm to μm range. Regarding nanowire research, the relatively fast imaging method is often utilized to obtain overview images of the nanowire structure as well as their dispersion and density on the underlying substrate.

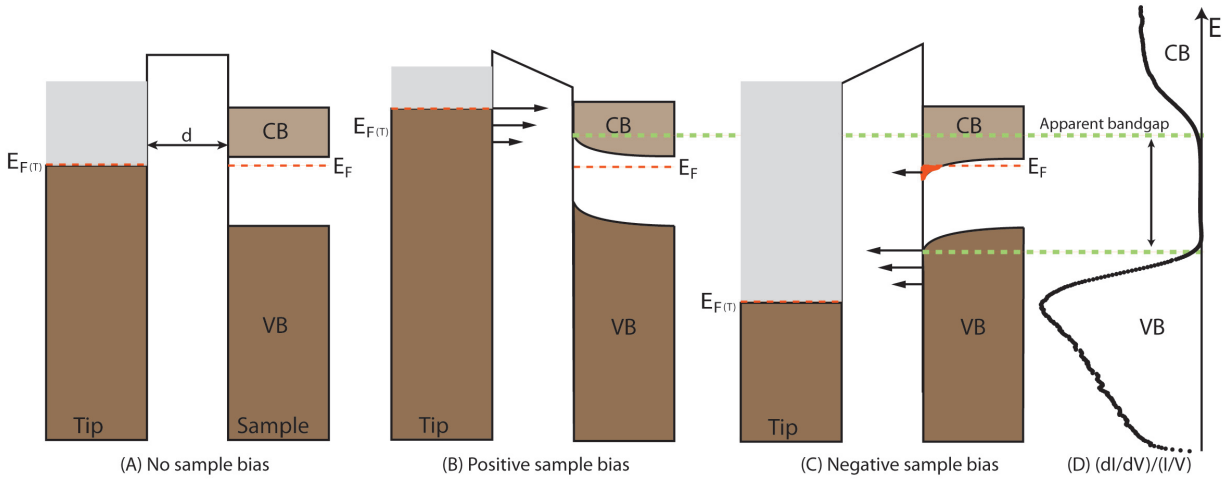

FIGURE 3.6. The image illustrates the results of band bending. In figure (A), no bias is applied resulting in aligned Fermi levels between tip and sample, and negligible band bending. In (B), a positive sample bias is applied, resulting in tunneling from tip to sample in addition to bending of the sample band structure. In (C), a negative bias is applied resulting in band bending in the opposite direction as well as tunneling from sample to tip. Due to the position of the Fermi level in the sample, additional states become available for tunneling (marked as red) as a result of the band bending. Figure (D) depicts a (dI/dV)/(I/V) spectrum with an apparent broadened band gap as a result of the band bending.

When imaging, the sample is irradiated by a well-focused beam of electrons which is raster scanned over the area of interest. As a result, several signals, such as backscattered as well as secondary electrons in addition to characteristic x-rays, are produced by the electron-sample interaction and collected by an analyzer. Each one of these signals can be used to obtain different information about the sample such as crystallography, surface topography and chemical composition [**44**].

For pure imaging purposes the secondary electrons, being the ionization product of inelastic scattering of the incoming electrons, are commonly used. Due to the limited mean free path of electrons in ambient conditions, SEM measurements are conducted in a vacuum chamber. All SEM images included in this thesis were obtained using a JOEL field-emission JSM6400F with a base pressure of 10^{-6} mbar.

CHAPTER 4

Nanowires

Nanowires are basically a highly ordered crystal structure in the form of a one dimensional freestanding rod, grown with high precision. The dimensions of nanowires comes in a wide spectrum, but their thickness can often be measured in tens of nanometers and the length in micrometers [**13**,**16**]. A property of such wires is the fact that the surface to bulk ratio greatly increases when working with spatial dimensions common for nanowires [**16**]. This invokes many interesting electronic features in the wires, highly treasured in the fast developing electronics industry [**3**], making them a viable target for scientific research.

Early nanowires only consisted of a single material, whereas the realization of heterostructures, i.e. wire composed of many different elements, is possible with current techniques [**3**].It is possible to grow heterostructures both axially as well as radially. The nanowires are typically hexagonal, resulting in a number of flat surfaces which atomic structure is defined by the crystal structure and growth plane. It is upon these facets that STM imaging is conducted. All nanowires investigated presented in this thesis were axially grown heterostructures consisting of InAs. Additional investigations of InP wires as well as GaAs wires were done, but the results are not presented here.

1. Nanowire growth

Nanowire growth is an epitaxial three stage process including mandatory steps such as metal alloy formation, nanowire nucleation followed by the actual growth stage. The nanowire growth material is often introduced in the form of a precursor, being vapor phase hydrides or organometallics containing the constituent element of the grown nanowire, and will under certain circumstances, involving temperatures and pressures, nucleate at specific sites. Typhical precursors are phosphine (PH_3), arsine (AsH_3) and trimethylindium ($TMIn$).

Commonly, catalytically active metall alloys, often in the form of Au droplets, will act as the above mentioned nucleation sites. The diameter of the Au particle will delimit the diamter of the nanowires. Hence, by controlling the Au particle size and concentration one can define the density and diameter of nanowires.

Although several growth techniques exist, such as *molecular beam epitaxy* (MBE), *chemical beam epitaxy* (CBE) and *metalorganic vapor phase epitaxy* (MOVPE) [**16**], the basic principles is analogous for all of them. Pre-growth, the substrate, commonly a semiconductor wafer cut in the (111)B direction due to superior growth properties of that crystal plane [**1**, **18**], is ridded of oxides. This step is followed by particle deposition, often done using aerosol techniques [**45**]

The actual nucleation and growth mechanism is often denoted as the *vapor-liquid-solid* mechanism (VSL) [**46**]. The name refers to the three aggregation phases involved in different

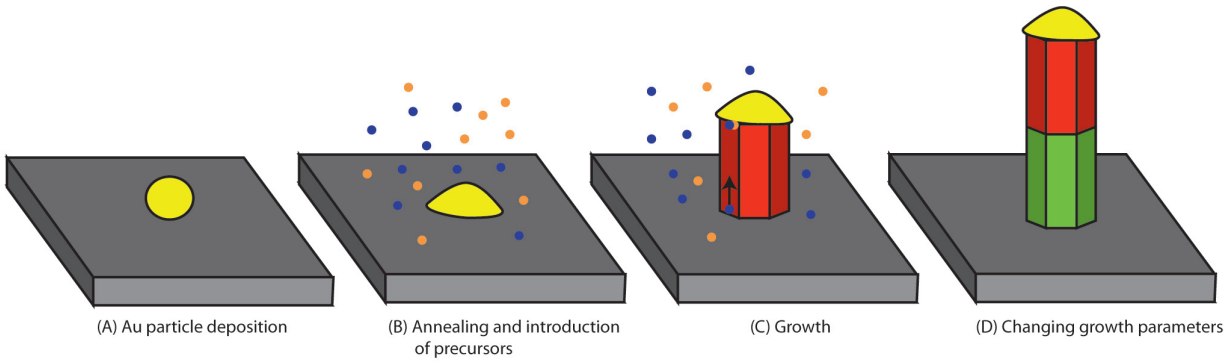

FIGURE 4.1. Schematic overview of the different stages involved in NW growth. In (A), the Au particles are deposited on the substrate. The size of the particle determines the diameter of the wire. In the following step, figure (B), the sample is annealed, melting the Au particle, and the appropriate precursors are added. This will result in nucleation at the interface between substrate and Au particle, ultimately leading to axial growth as illustrated in (C). By changing parameters, such as pressure, precursor specie or temperature, axial heterostructures can be created as depicted in (D).

stages of the growth. After introduction, the vapor phase precursors will decompose and alloy with the liquid phase Au particle if heated. This will result in a supersaturation of group III material in the Au particle. The growth temperatures, usually in the range of 4-500 ℃, are maintained such that the Au particle remains in its liquid state for the whole growth procedure [**47**].

When supersaturation is reached, the NW elements will precipitate at the liquid/solid interface, leaving only the group III or V element. This process is continuously repeated, displacing the Au particle from the substrate, lifting it upwards, as more and more material is deposited at the interface [**47**]. Hence, the Au particle will always be located on top of the nanowire. When the VSL mechanism is initiated, the precursors will actually condense at the bottom of the wire and diffuse, up along the nanowire, towards the Au particle, where the growth is continued. When diffusing along the wire, some precursor material will dissolve, resulting in a slight radial growth of the nanowire.

Since the lower part of the wire will be exposed to the growth material for a longer time, its diameter will be somewhat larger than the upper part. This will lead to cone shaped wires perpendicular to the growth substrate. This phenomenon is often referred to as tapering, and can be estimated in number of atomic steps per unit length along the wire. In order to avoid major tapering, the wires are often etched simultaneous to the growth procedure. The etching is more volatile at the thicker part of the wires, finally resulting in a rod shaped wire with substantially less tapering.

When the growth is halted and the temperatures decreased, the Au particle solidifies. Due to the alloying process, i.e. adding material, the final diameter of the wires will have a slight difference with respect to the original diameter of the Au particles [**47**]. The growth procedure is briefly illustrated in fig. 4.1.

Although particle assisted growth is the most common method, other options are available such as *self-assembled organic films* [**14**, **48**]. Such growth methods might be preferable since Au has been reported to induce unwanted deep levels in for instance Si [**14**]. Additionally there have been reports of III-V nanowires being dissolved by Au particles.

As described in detail in [**14**], the growth material itself will form the catalytic particles enabling the VSL growth in this method. In order to enable the formation of such particles, a Si substrate is coated in organic material after the removal of oxides. However, due to irregular thickness of the coating film, some parts of the substrate will be vulnerable to re-oxidation, forming SiO_2. When annealing, the organic film will be evaporated, leaving spots with SiO_X which are preferable for nucleation, whereas the patches of SiO_2 will inhibit growth.

CHAPTER 5

Sample preparation

Regarding STM studies on nanowires, the nanowire side facets are the main focus of interest. Therefore it is required to orient the wires such that the probing tip can easily access them. In addition, when transferring the nanowires from the growth chamber to any research facility, native oxides will form and cover the surface. This is problematic since no STM can be performed on such surfaces due to low conductivity related to oxides. In addition the surface of interest cannot properly be probed since it is covered with oxides. This chapter will briefly describe the transfering and deoxidation process of the InAs nanowires studied.

1. Nanowire transfer

In order to study the side facets of nanowires with an STM, the facets must be oriented such that an STM tip can probe them. Since nanowires originally grow perpendicular to the growth substrate, this poses a problem. This is solved by breaking the wires and placing them horizontally on a suitable substrate.

Regarding the transfer, there are a certain number of criteria that should be fulfilled in order to simplify the scanning process. First of all, the wire coverage of the surface should be as high as possible, making them easier to locate. However, a very high concentration will cause the nanowires to bundle together, posing a big problem when performing STM due to the height of such bundles. In addition, the wires should only break off at the base of the nanowire, since it is very hard to separate nanowire fragments from actual nanowires when performing STM. It is therefore advisable to study the surface coverage after deposition with a SEM in order estimate the fragment and wire density.

The transfer itself is done by having mechanical contact between the growth sample, with the freestanding nanowires, and the substrate sample used for STM studies. The wafers are gently pushed against each other, ensuring that most break offs occur at the bottom of the wires. This method, called *proximity transfer*, was developed by Martin Hjort at Lund University and has been proven to fulfill the above given criteria in a more suitable way than other transferring methods such as the *clean room wipe trasfer* method [**17**].

Usually the nanowires are transferred to a substrate consisting of the same material as the wires. This is to ensure that the formed oxides of the substrate surface and nanowire surfaces are similar, simplifying the deoxidation process.

2. Deoxidation

The conventional ways to remove oxides are either by sputtering or thermal cleaning. The latter one is the only viable method when considering nanowires, since sputtering would destroy the nanowires. The principle of thermal cleaning is to anneal the sample to temperatures required for the oxygen species to desorb. Unfortunately, those temperatures are often

much higher than the congruent evaporation temperature for III-V semiconductors such as InAs, which evaporates at 380 ℃ [**16**].

This problem is solved by exposing the oxides to atomic hydrogen in parallel to moderate heating of the sample, i.e. 360-380 ℃for InAs. The hydrogen will interact with the oxides, forming more volatile species with reduced desorption energy barriers, making desorption possible at reduced temperatures.

The atomic hydrogen is created by cracking molecular hydrogen by the use of a filament heated to approximately 2000 ℃. Due to the low kinetic energy of the formed hydrogen radicals, only the surface of the sample should be affected, ensuring that no hydrogen will be incorporated in the wires [**13**].

After the deoxidation process, the sample must remain in UHV conditions in order not to reoxidize immediately. Even when kept in UHV, the sample will eventually reoxidize, but by having pressures in the 10^{-11} mbar regime the sample can usually stay clean for about a week.

Part 2

Experiments and Results

CHAPTER 6

Crystal Engineered InAs Nanowires

1. Experimental

Crystal engineered InAs nanowires, consisting of a WZ and ZB heterostructure, were grown, utilizing the MOVPE method in conjunction with conventional Au particle seeding. The Au particles were deposited using an aerosol technique [**45**] onto a (111)B oriented InAs substrate, resulting in an areal density of 0.5 and 1.0 μm^{-2} and particle diameters in the range of 50-80 nm. Respective precursors, trimethylindium (TMIn) and arsine (AsH_3), were introduced when the growth temperature of 460 ℃was reached. The growth was executed in an AIXTRON 200/4 system using a total reactor flow of 13 *standard liters per minute* (slm).

A 10 minute anneal at 550 ℃, in an AsH_3/H_2 atmosphere was performed prior to growth in order to remove surface oxides. Following this, the temperature was reduced to the given growth temperature, and upon thermal stabilization, growth was initiated. Post processing involved cooling in an AsH_3/H_2 atmosphere in order to avert thermal decomposition of the wires. The resulting well defined polytypic wires with varying, but well defined, axial stacking of WZ and ZB were evaluated with STM as well as STS. The heterostructure periodicity was determined by precisely tuning the marginal V/III-ratio of according precursors.

The parameters where such that the ZB segments would form well-spaced TSL, with (111)A/B termination, which would during the growth process be more or less overgrown, exhibiting a ZB{110} facet rotated with respect to the (111)A/B facets as illustrated in fig. 6.1. Due to growth parameters the uppermost TSL segment was believed to be clear from overgrowth, and hence a valuable target for spectroscopy. The wurtzite segments were expected to originally be terminated by $\{10\bar{1}0\}$, but as the growth progressed be overgrown resulting in either $\{1\bar{1}00\}$ or $\{11\bar{2}0\}$ facets. Investigations of the mentioned facets are of special interest since WZ growth of III-V crystals, and corresponding facets, solely occurs in nanowires [**10**], and have yet to be seen in bulk form.

As required for STM studies, the wires were broken of and deposited on a substrate, using the close proximity method [**17**]. The substrate used was an n-doped InAs(111)B substrate, cut from the same wafer for all samples looked at. Removal of native oxides, due to exposure to ambient conditions, was performed by annealing the samples to 380 ℃in an atomic hydrogen atmosphere with a pressure of $2 \cdot 10^{-6}$ mbar, which previously has been proved successful [**16**]. Cleaning times varied between 20-40 minutes between different samples in accordance to previous successes.

In order to map the overall structure and morphology, as well as identifying the different facets, images were taken in series while stepping along the nanowire. Those were later composed into a single image in order to be compared to SEM images, see fig. 6.4. Such

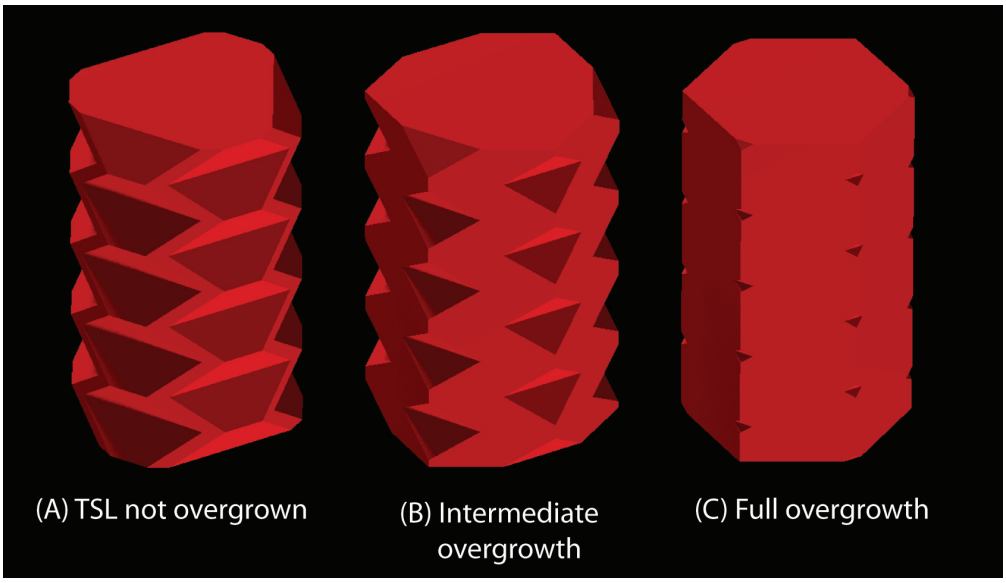

FIGURE 6.1. A 3D model of a TSL segment illustrated at different stages of ZB{110} overgrowth. As seen in a) the {110} facet is originating in between two TSL segments, being rotated with respect to those. As the overgrowth continuous in b), the {110} facet growths wider at the cost of the {111}A/B facets of the TSL. In c) the overgrowth is almost complete, and almost only {110} facets can be seen, rotated 60 degrees to each other. Image made by Sebastian Lehmann from Lund University.

an overview is invaluable when traversing along the wire, aiming to find the target facet of interest in addition to determining the growth direction and orientation of the wire.

2. Results

The amount of results presented below requires a certain degree of structuring. Hence, this section is divided into four parts which individually will tangent different topics. First, a short overview regarding the various facet structures identified along the nanowire is given. This section is followed by a description of the overall 3D morphology, and how it changes along the wire, presented in the form of a model. The model is partly based on observations presented in the third part of the results, regarding the actual surface structure of each facet type. Finally the electronic properties, based on STS experiments, of the nanowire will be reviewed. All these results will lastly be concluded into a short summary in order to bind them together.

2.1. Facet characterization. Facet identification was done by obtaining atomically resolved images on the given facets. Such images, displayed in fig. 6.2, were obtained on all surfaces except the TSL {111}A/B facets, on which only semi-atomic resolution was achieved. TSL has however been studied in detail before [**6**, **12**, **18**], in addition to having a very distinct morphology, and can thus easily be identified as such.

Although atomic resolution is required in order to originally establish the facet type, it was found that even at a large scale the morphological differences between the facets were

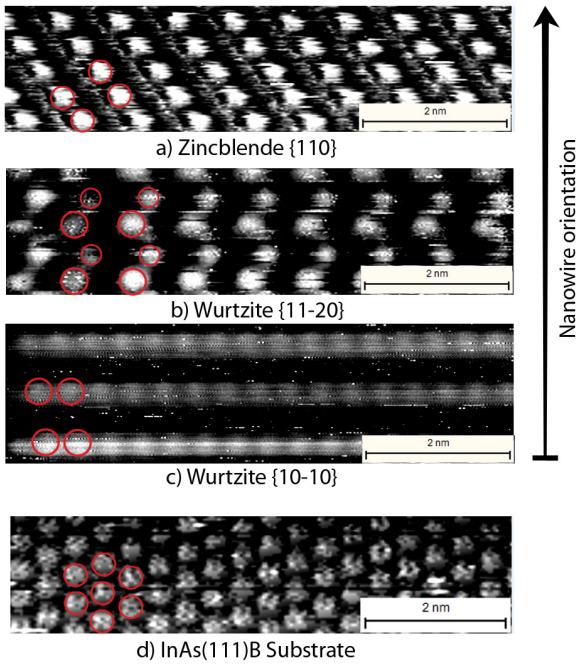

FIGURE 6.2. The figure displays an overview of the atomic lattices of the different facets seen on the wire. An exception is the {111}A/B facets of the TSL at which we were unable to obtain atomically resolved images. However, the atomic structure of the {111}B substrate is included as a reference. Every second atom of the $\{11\bar{2}0\}$ plane often appeared to be smaller, a feature attributed to spatial orientation of the dangling bonds of the atoms. The atomic structure of the $\{10\bar{1}0\}$ facet if figure (c) has in reality a square lattice. The distortion seen in the figure is attributed to drift.

big enough for identification, as seen in fig. 6.3. The imaged structure in fig. 6.3a can easily be identified as ZB TSL due to the sawtooth structure consisting of alternating {111}A and {111}B ZB facets, with a relative angle of 60°. On both sides of the sawtooth structure, {110} facets exhibiting a zig-zag contour in correlation with the shift from {111}A into {111}B can be seen, indicative of overgrowth of the TSL. Due to the relatively small degree of overgrowth, i.e. facets being thin, it is believed to be the uppermost, towards the gold particle, of the ZB segments, denoted as region I if fig. 6.4.

Fig. 6.3b depicts one of the lower and hence more overgrown ZB TSL segments. Note that the perspective of this imaged is rotated 30°relative the TSL segment in fig. 6.3a and only the {110} facet can be seen. The nagged edges of the facet can be regarded as the {111}A/B facets seen in a 30°profile. In this section of the wire the facet has grown a lot wider, with a diameter of roughly 80 nm in contrast to the 15 nm facet seen in fig. 6.3a. In addition, the zig-zag edges of the facet are no longer as distinct and well defined, indicative of a considerable overgrowth of the {111}A/B facets. To the right in the image a transition into WZ$\{11\bar{2}0\}$ can be seen, marked out by the arrow.

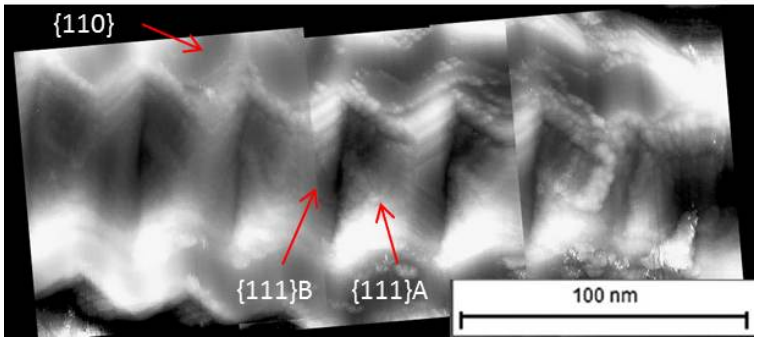

(A) TPS

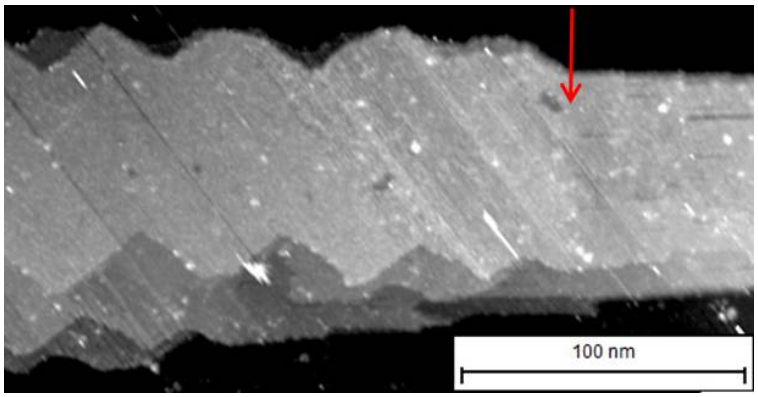

(B) ZB{110}

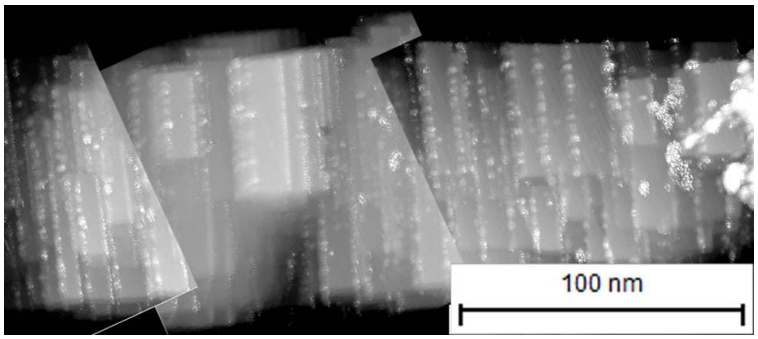

(C) WZ{10-10}

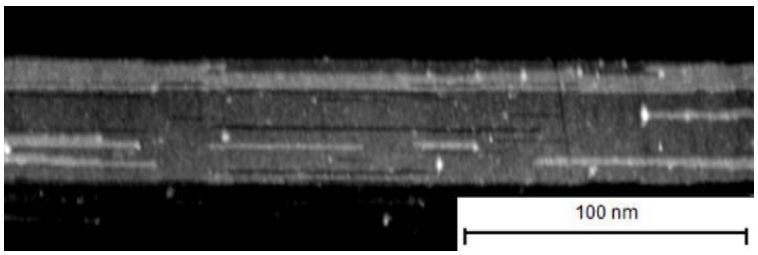

(D) WZ{11-20}

FIGURE 6.3. The figure includes overview STM images of all the facets found on the wires. A distinct morphological difference between the different facets can be seen. *The images were all obtained using filled state imaging.*

The WZ$\{10\bar{1}0\}$ facets, seen in fig. 6.3c, can easily be identified due to frequent sharp atomic steps, always perpendicular to growth direction, resulting in a stair like appearance of the wire and a lot of tapering. All such steps seen during this study were covered by a line of adsorbants, henceforth denoted as *sausages*, and were one or several atomic layers high. However, not all of the sausages were correlated to atomic steps, as clearly seen in fig. 6.11a and 6.11b, something which is discussed in detail later. Hence, this surface mainly consists of numerous micro facets with WZ$\{10\bar{1}0\}$ structure, separated by the mentioned sausages.

Always in a 30°rotaion relative the WZ$\{10\bar{1}0\}$, but aligned with the ZB$\{110\}$, is the WZ$\{11\bar{2}0\}$ structure, which is depicted in fig. 6.3d. This surface is characterized by relatively few atomic steps, but with a finger like growth stretching along the wire where one or several atomic rows are missing from a surface layer, seen as dark stripes in the figure. The opposite was also observed, meaning an incomplete surface layer consisting of only a few of atomic rows, seen as bright stripes in the figure. The thickness of these fingers can be everything from one atom up to several 10s of atoms, and can stretch more than 100 nm along the wire. The height of the fingers was always observed to be only one atomic layer.

Hence, all observed facets have a very distinct and individual surface morphology and can thus be identified without the requirement of atomic resolution. Identification is aided further by knowing the relative rotation between the different crystal planes. Such information was vital when reviewing data regarding the nanowire facet structure, which ultimately led to the model presented below. in fig. 6.4.

2.2. 3D morphology. An overview SEM image of the studied nanowires, revealing that the conformation indeed is heterostructural, is displayed in the left section of fig. 6.4. Due to the complexity of the nanowire structure different sections of the wire have been designated I-VI and will be discussed separately. Regarding general crystal structure however, the wires have 3 WZ segments and 3 ZB segments, alternated by each other, starting with a WZ segment at the bottom. Despite identical growth conditions for each segment, their respective facet structure might not be. The difference between analogous regions will depend on the relative degree of overgrowth they experience in parallel to axial growth. Hence it should be noted that region I, III, and V originally had the same structure, but due to overgrowth exhibit different facet properties or terminations. For example, the WZ segment of region II might exhibit different facets than the equivalence of region VI since it has been exposed to growth conditions for a longer time period. Region IV should hence be in a state in between the other two. The same applies for the ZB segments I, III and V.

Also depicted in fig. 6.4 is a model of the facet structure for each region of the wire. The model should be considered as a flattened wire as illustrated by the scale bar at the bottom, showing angles from 0°to 360°. Each color in the figure represents a different facet type. Crossections of the wire in certain regions are marked with a black arrow and are denoted A, B, C, D and E in the figure.

The model is based on numerous observations from SEM as well as STM images, but was mainly constructed by utilizing composite STM images such as the one shown to the right in fig. 6.4, which includes section II to V of the wire. The difference in length of the wire imaged with SEM respectively STM can be explained by individual variations related to growth, as well as piezo drift during scanning.

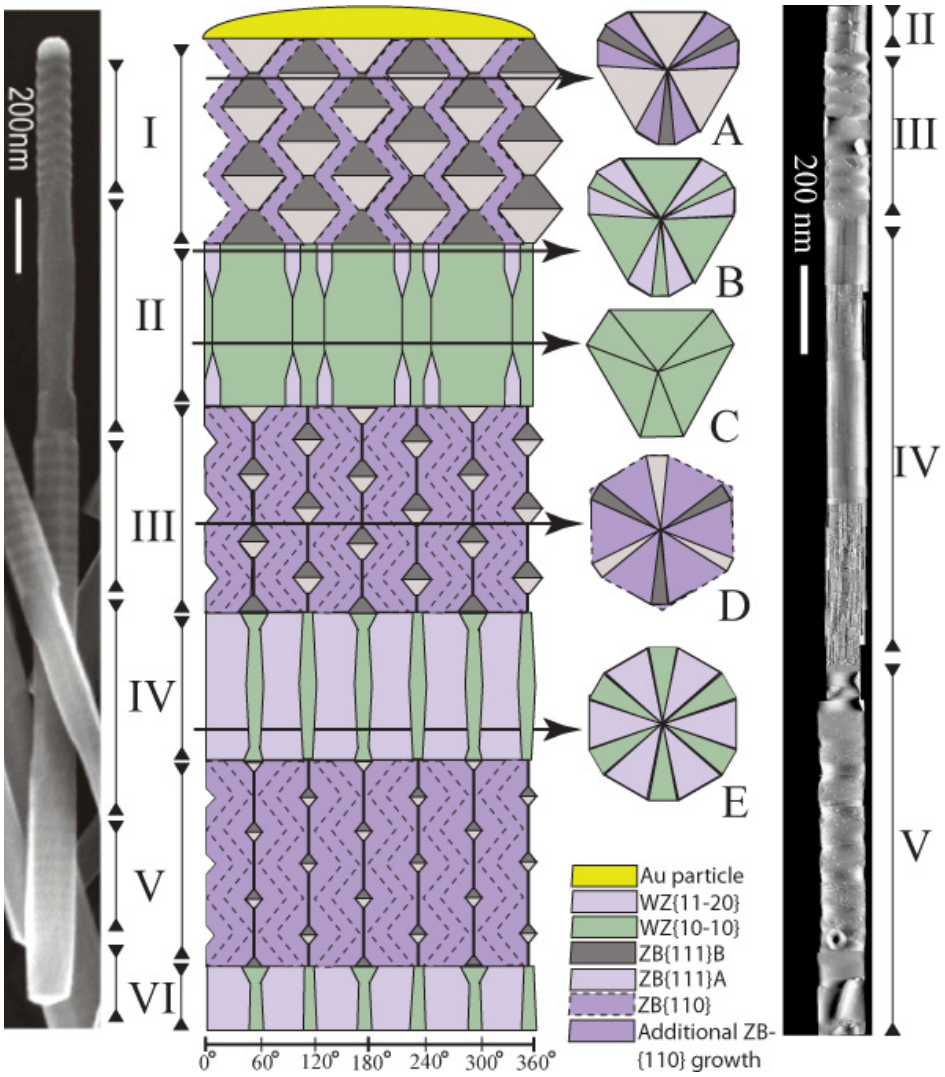

FIGURE 6.4. The figure depicts a SEM image (left), mapping out the different crystallographic regions of the nanowire, as well as a suggested model (middle) of the relative facet structure along the wire. A composite STM image can be seen to the right in the image; corresponding parts of the wire are marked out. The model should be considered as a nanowire being flattened out. The black arrows indicate a crossection of the wire which are denoted as A, B, C, D and E in the figure. In the image, region I corresponds to the uppermost part of the nanowire, being mainly ZB TSL with some slight ZB{110} overgrowth. Section II has a WZ crystal structure with dominating $\{10\bar{1}0\}$ facets, separated by each other by thin $\{11\bar{2}0\}$ facets as a result of overgrowth. Section III and V are both in analogy with the structure in section I, but the {110} overgrowth has progressed further. In reality the lower segment, V, should be more overgrown than the middle ZB segment, III, exhibiting little to no remnants of the underlying TSL structure. Region IV and VI of the wire consists of 12 facets, being alternating WZ$\{10\bar{1}0\}$ and WZ$\{11\bar{2}0\}$, with the latter being the largest.

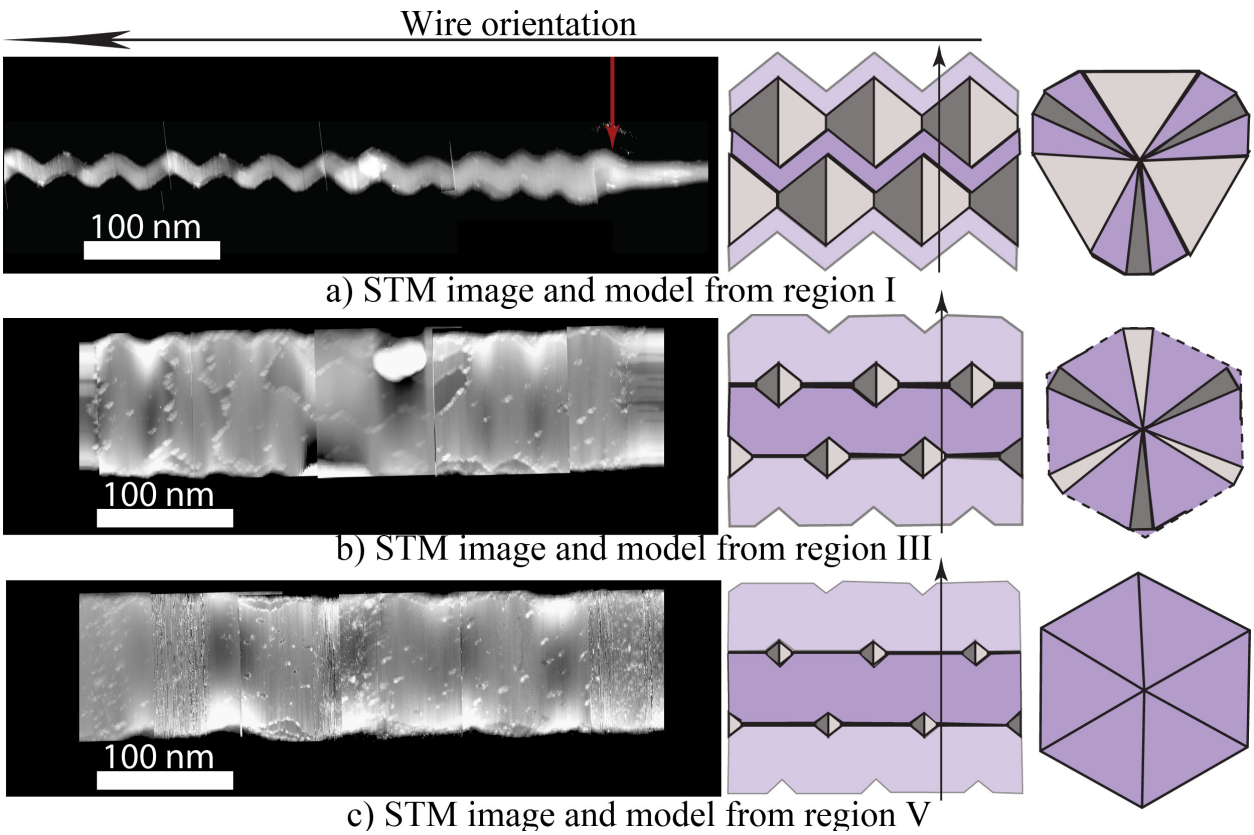

FIGURE 6.5. The figure depicts ZB{110} facets from both region I (a), III (b) and V (c) of a nanowire. Parts of the model, including crossections, presented in fig. 6.4 are shown to the right of each image. The corresponding facet represented is highlighted by having a brighter color than adjacent facets in the model. The relative overgrowth between the three regions is quite apparent. In image from region I has a very distinct zig-zag profile, and in addition is very thin, suggesting a very slight overgrowth just barely initiated. The number of steps in the image from section III are numerous, whereas there are none in the image portraying the facet from region V. In addition, the edges of the facet in the middle image (b) are still relatively nagged, suggesting that some remnants of the TSL still should be present. The edges of the image in fig. b) are however almost straight, only showing a hint of being nagged, signifying an almost complete overgrowth with little to no remnants of the TSL.

A description of the morphology and facet structure of each region, in addition to transitions into adjacent regions, is given below. The regions will be referred to by using the designation system from fig. 6.4, numbering them from I-VI.

Region I, being closest to the gold particle, was found consisting of large {111}A and {111}B facets alternating each other, creating a sawtooth morphology as in fig. 6.3a. This periodic alteration between such facets is commonly correlated to twinning superlattices (TSL) [**9**], and results in a hexagon, where each side exhibits the mentioned sawtooth morphology, as illustrated in fig. 6.1a. Adjacent to the sawtooth structure, and rotated

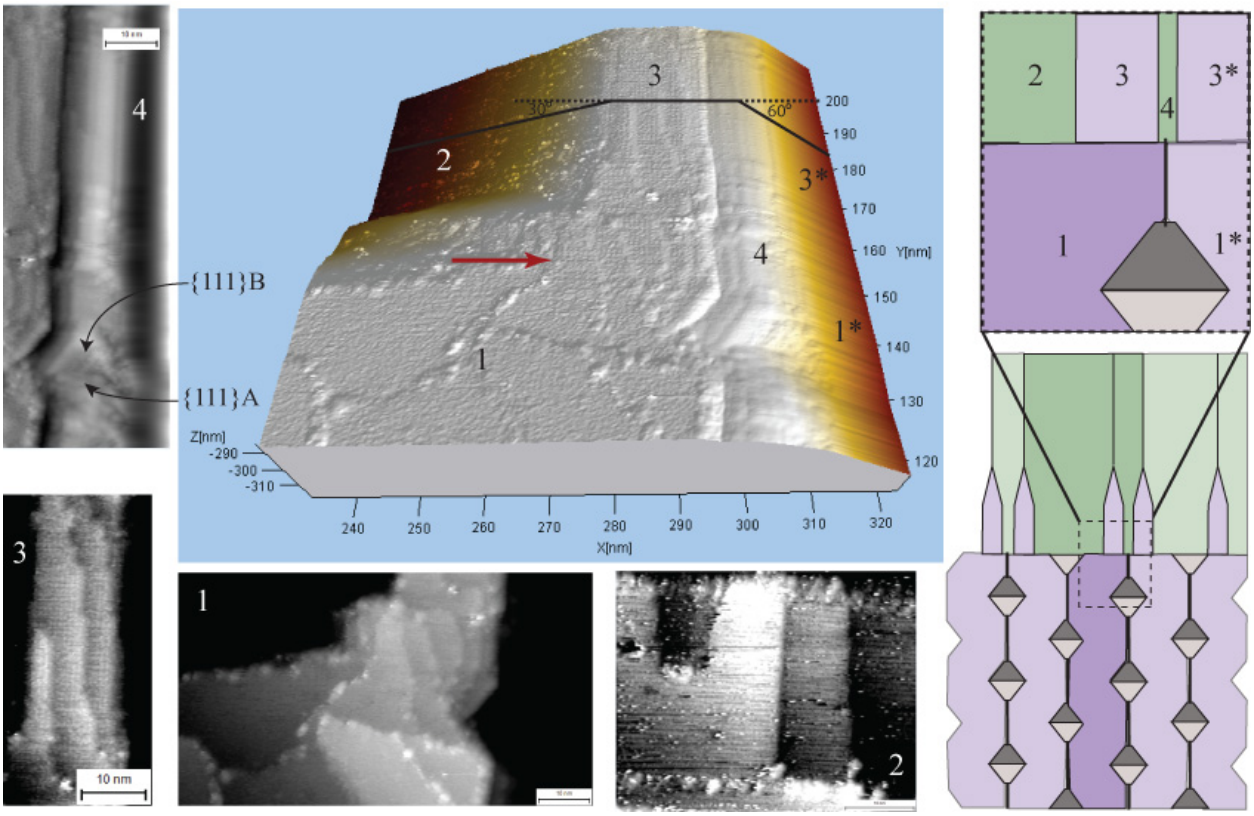

FIGURE 6.6. The figure depicts a 3D representation of an STM image corresponding to an area marked by the dashed square in the model to the right. The numbers 1, 2, 3 and 4 in the 3D figure represent different facet types being ZB{110}, WZ{10$\bar{1}$0}, WZ{11$\bar{2}$0} and ZB{111}A/B going into WZ{10$\bar{1}$0}, respectively. Each of these facets are shown as regular STM images with corresponding designations. The asterix, i.e. 1^* and 3^*, suggests that a corresponding facet is located at that position, but rotated 60°with respect to the original facet represented by the specific number.

30°relative to those, very thin, around 10 nm, zig-zag facets terminated by {110} were found. Their presence is attributed to overgrowth of the {111}A/B facets, as is visualized in fig. 6.1. The zig-zag profile is attributed to the underlying {111}A and {111}B facets, since the overgrowth will adapt the underlying twinning structure.

The overgrowth was found to extend throughout the whole ZB segment, all the way to the gold particle, see fig. 6.5a, suggesting that the overgrowth is initiated at an early state in the growth of the ZB segment. If not, the uppermost twin segments would not have experienced any overgrowth. Hence, as depicted in the model of fig. 6.4, this portion of the wire was found to consist of 6 {110} facets and 6 facets exhibiting the sawtooth structure, alternating each other.

The other ZB regions, III and V, were found to have an analogous appearance except the degree of overgrowth, being greater for the two, as can be seen in fig. 6.5. The degree of overgrowth has a strong correlation to the exposure to growth conditions of a single segment,

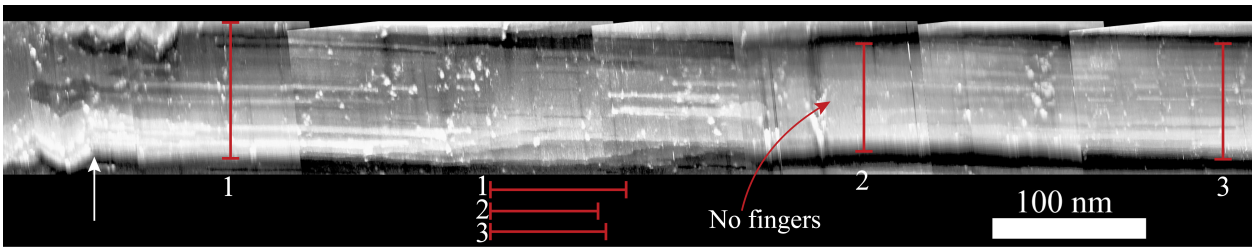

FIGURE 6.7. The figure depicts a composite STM image of a $\{11\bar{2}0\}$ facet. To the right, indicated by the white arrow, the transition into ZB$\{110\}$ can be seen. The fingers can be seen stretching out from the interface several hundred nm. The red scale bars, denoted 1, 2 and 3, indicate the facet thickness at their corresponding locations. It is clear that the thickest part is close to the interface, whereas the thinnest part is in the middle of the WZ segment. The fact that the facet is getting thicker to the right, scale bar 3, suggests that it is close to another WZ/ZB interface. In the middle of the segment no finger growth can be observed, marked by the red arrow, suggesting that fingers from both interfaces meet at this point, creating a complete $\{11\bar{2}0\}$ layer.

explaining why region V is more overgrown than both I and III. In relation to each of the images in fig. 6.5 parts of the model, representing associated region, are illustrated.

Further analysis yields that the $\{110\}$ facet in fig. 6.5b exhibits numerous steps as well as island growth, suggesting a still incomplete overgrowth. In addition, the edges still display a zig-zag profile, although not as distinct as in fig. 6.5a, furhter suggesting an incomplete overgrowth. Hence, a crossection of that part of the wire would not yet be truly hexagonal, as is shown in the figure.

Fig. 6.5c however, does not display any atomic steps and next to no remnants of the underlying TSL can be seen in the form of zig-zag edges. Hence, it is quite plausible to conclude that the ZB segment of region V is almost completely overgrown, as illustrated in the suggested model, resulting in a truly hexagonal crossection.

Although all the ZB segments appear to be essentially equal regarding facet structure, except for the thickness of the different facets, this however does not apply for the WZ segments as reflected in the model. Originally all WZ segments were constructed by 6 facets, all with the $\{10\bar{1}0\}$ termination, and a relative rotation of 60°. A crossection of such a segment is depicted as C in fig. 6.4. However, region II was for instance found to be dominated by the original $\{10\bar{1}0\}$ facets, with a thickness in the order of 80 nm, but bordered by thin $\{11\bar{2}0\}$ facets, with a width of about 15 nm, on each side. This is based on findings of such facets close to the ZB/WZ interface, as can be seen in fig. 6.5a and fig. 6.6. The latter figure displays a 3D representation of an STM image, portraying a transition from region III, being ZB, into region II, being WZ.

Four different facet types were found in the image, marked as 1, 2, 3 and 4, being ZB$\{110\}$, WZ$\{10\bar{1}0\}$, WZ$\{11\bar{2}0\}$ and ZB$\{111\}$A/B going into WZ$\{10\bar{1}0\}$, respectively. Each of these facets are also shown in the figure as regular STM images with corresponding designations, as well as being marked out in the model. The characteristic morphology of each surface was used as identification in those cases.

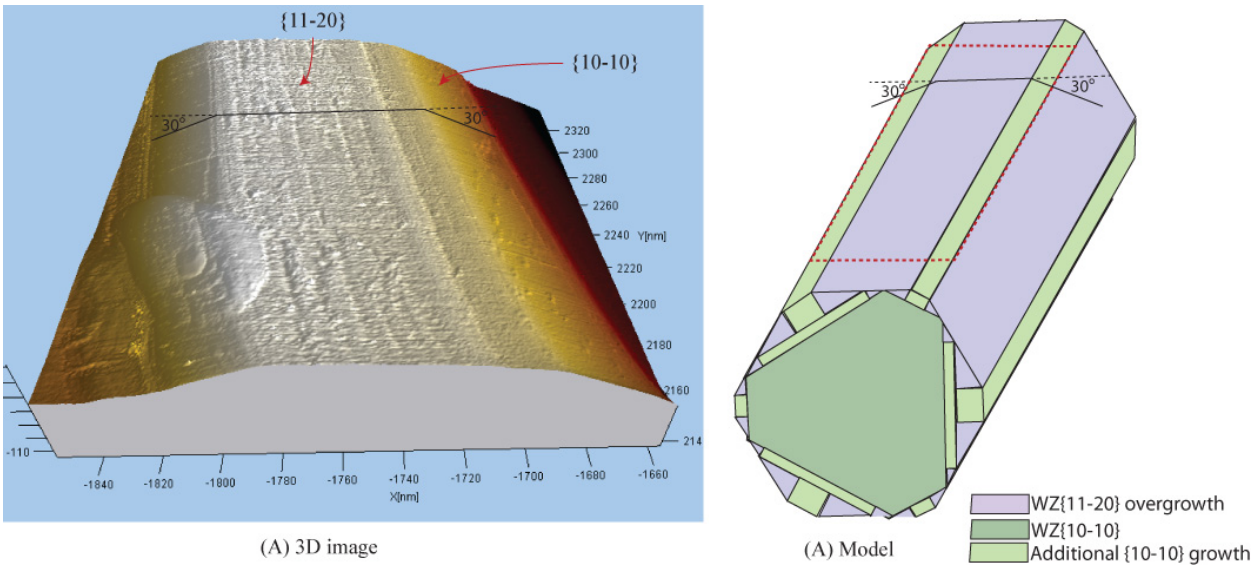

FIGURE 6.8. In the figure a 3D representation of an STM image can be seen, (A), as well as a 3D model of the believed facet structure of the imaged region, (B). The STM image depicts a $\{11\bar{2}0\}$ facet adjacent by $\{10\bar{1}0\}$ facets, both rotated 30°relative to the $\{11\bar{2}0\}$ facet, on both sides. The region imaged in figure A is represented by the dashed (red) region of the model in figure B.

As can be seen in the figure, there is an expected 30°rotation between the $\{10\bar{1}0\}$ facet and the $\{11\bar{2}0\}$ facet, confirming those as such. Facets designated with a digit with an asterix were not directly observed, but identified as a facet corresponding to the given digit with the help of measured angles. For instance, Since a measured angle of 60°was found between facet 3 and 3^* both of them must be WZ$\{11\bar{2}0\}$. The same applies to facet 1 and 1^* which both must be ZB$\{110\}$ facets.

Based on the observations in this image, a suggested model was created regarding the associated region of the wire, and can be seen to the right in fig. 6.6. The area imaged in the 3D representation is marked out by the dashed square in the model. Weather the $\{11\bar{2}0\}$ segment extends throughout the whole WZ segment is uncertain, and will be further discussed later.

These findings do however suggest that at least parts of section II of the wire, close to the ZB/WZ interface, would consist of 6 $\{11\bar{2}0\}$, and possibly 6 $\{10\bar{1}0\}$ facets, with 3 of them being very large (100 nm) and 3 extremely thin (10 nm), bringing it to a total of 12 possible facets. A corresponding crossectional image is depicted as B, in fig. 6.4.

Comparable observations were done by Xu *et al.* on similar nanowires, consisting of InAsSb and having a double heterostructure starting with a WZ segment followed by a twinned ZB segment. They attributed the presence of $\{11\bar{2}0\}$ facets to self overgrowth due to prolonged exposure to growth conditions, resulting in the formation of favored $\{11\bar{2}0\}$ facets [**9**].

However, only the parts close to the ZB/WZ interface were found to exhibited the $\{11\bar{2}0\}$ facets in their study. If the overgrowth was related to extended growth times, the lower WZ segment should be even more overgrown than the higher located one, which was not observed.

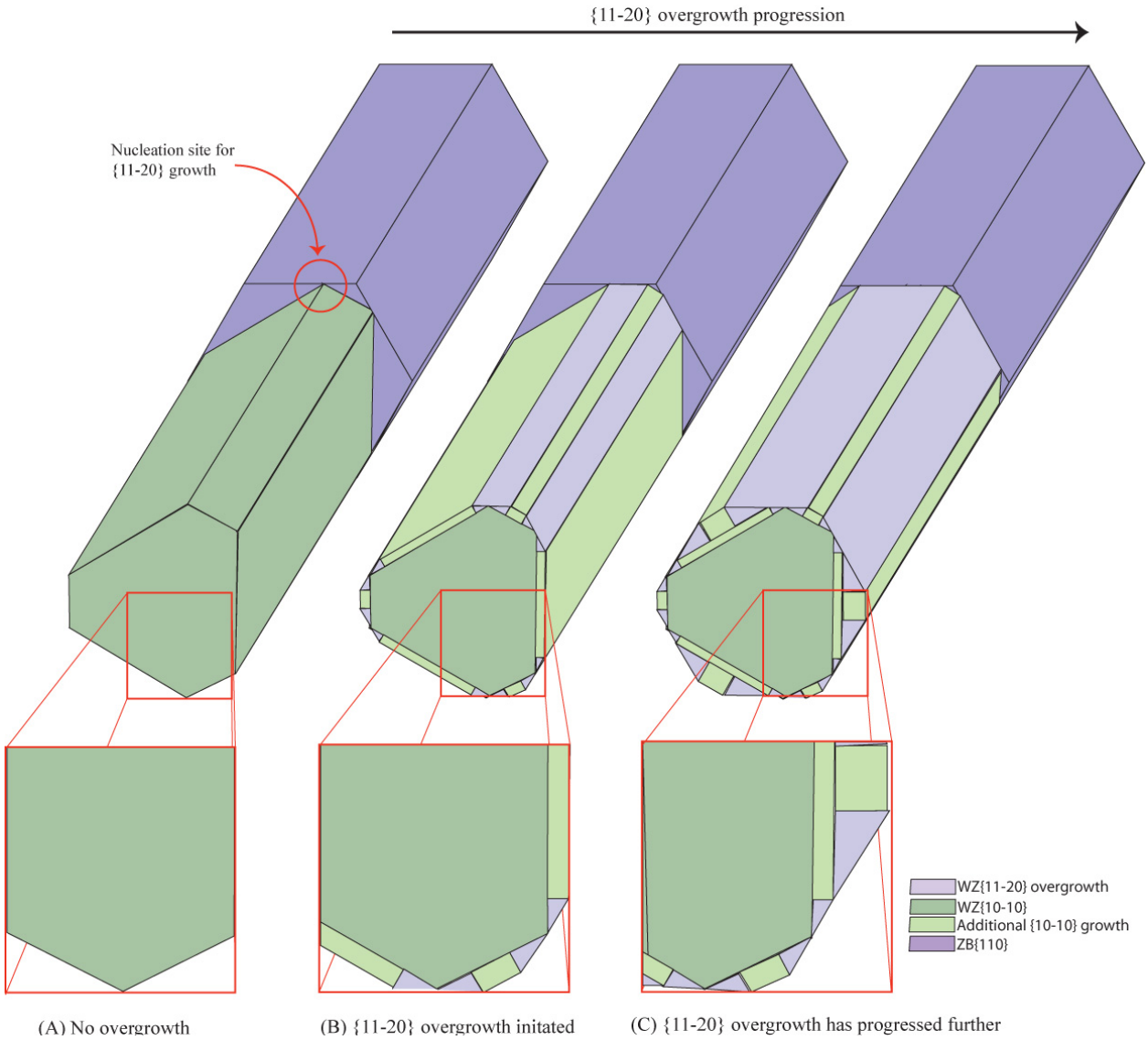

FIGURE 6.9. The figure illustrates how the $\{11\bar{2}0\}$ facet is formed due to overgrowth of the $\{10\bar{1}0\}$ facets. As marked by the red circle, the interface between the WZ$\{10\bar{1}0\}$ and the ZB$\{110\}$ facets is believed to be the nucleation site for the growth. As the $\{11\bar{2}0\}$ growth progresses throughout figure (A), (B) and (C), the $\{10\bar{1}0\}$ facet is believed to grow radially in parallel. This can more clearly be seen in the inset figures marked by the red squares.

On the contrary, those parts consisted solely of the original 6 $\{10\bar{1}0\}$ facets. This was explained by competitive process between the radial growth of the wire and incorporation of adatoms at the base of the wire. In contrast to their study, STM images of region I suggested that the $\{11\bar{2}0\}$ segment extended along the whole WZ segment, based on the fact that such facets were observed at the WZ/ZB interface between both region I and II, see fig. 6.5, as well as II and III, fig. 6.6.

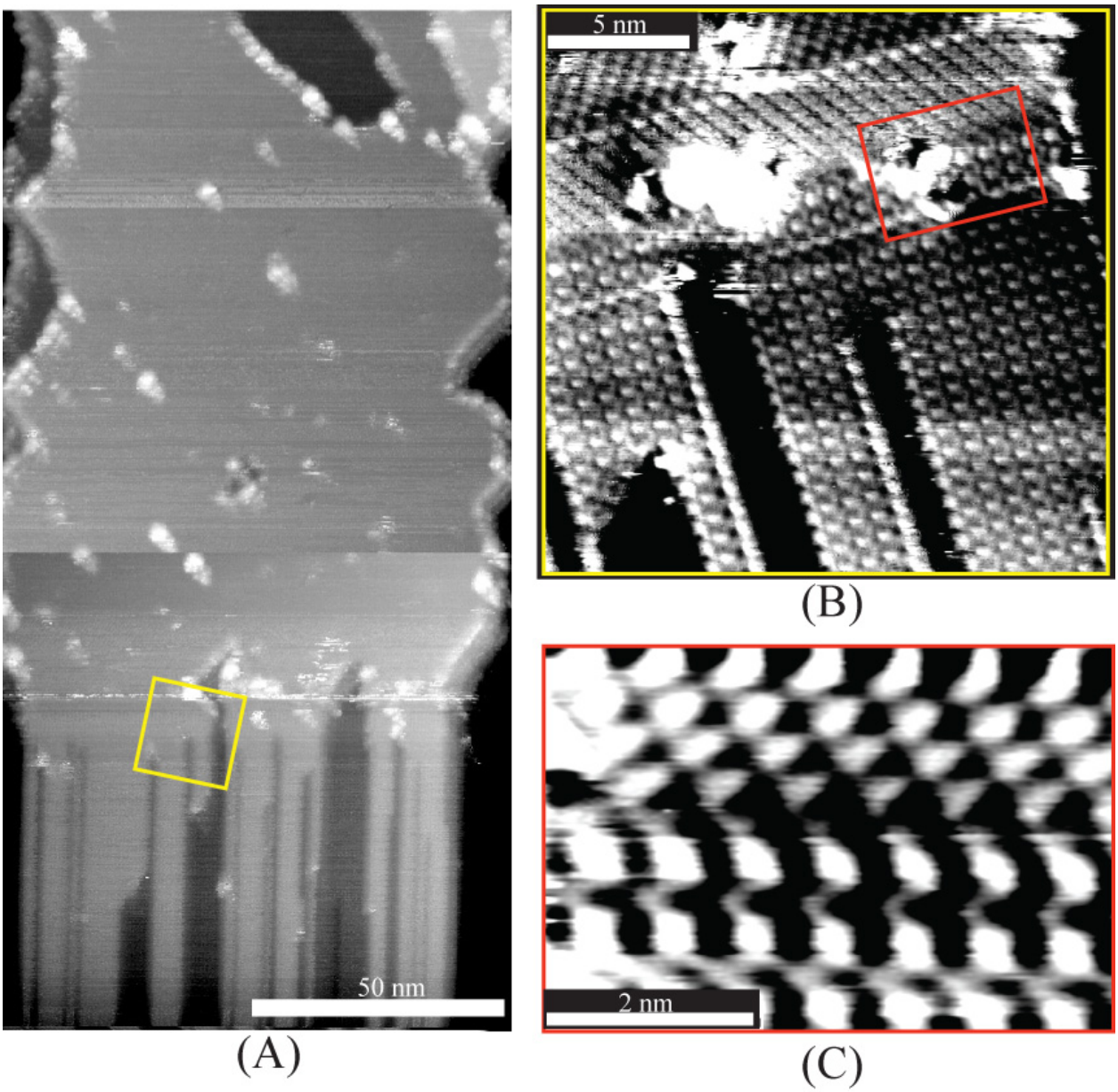

FIGURE 6.10. The figure depicts the transition from ZB{110} into WZ{11$\bar{2}$0} at different magnitudes, as indicated by the scale bars. The approximate area of figure (B) is marked out by a yellow square in figure (A). In analogy, the area of figure (C) is marked out in figure (B), but as a red square. Both figure (B) and (C) exhibit atomic resolution.

Another viable explanation could be related to the absence of favorable nucleation sites for the initiation of {11$\bar{2}$0} growth at the lower part of the WZ segment in the study by Xu *et al.*. Such sites could however be provided at the WZ/ZB interface, explaining why {11$\bar{2}$0} facets were found adjacent to those, as illustrated in fig. 6.9.

Regarding the latter explanation, it is quite plausible that the $\{11\bar{2}0\}$ segments of region I do not extend along the whole WZ segment, deeming on the relatively small thickness of the facets, but rather extend out from the interface a limited length as illustrated in the model. Assuming this to be correct, the $\{11\bar{2}0\}$ segments of region IV and VI should be more overgrown, and possibly meet in the middle between the two ZB segments, and persist throughout the whole WZ segment. The resulting $\{11\bar{2}0\}$ facet would however be thinner in the middle between two ZB segments. This was generally observed when scanning on the $\{11\bar{2}0\}$ facets, and a composite STM image of a WZ$\{11\bar{2}0\}$ facet from region IV depicting precisely that can be seen in fig. 6.7.

A result of the wide $\{11\bar{2}0\}$ facets in region IV and VI, would be that the $\{10\bar{1}0\}$ facets would be correspondingly thinner, or possibly completely overgrown. The relative size between the facets can clearly be seen in fig. 6.8, depicting a 3D representation of an imaged WZ section of the wire. As can be seen in the figure, the $\{11\bar{2}0\}$ facet, having a width of about 80 nm has two thin, being only about 30 nm wide, $\{10\bar{1}0\}$ facets on either side. As expected between two such facets, a 30°rotation was found relative them. The fact that the $\{10\bar{1}0\}$ facets have a significantly reduced width compared to their equivalences in region II does indeed suggest that the $\{11\bar{2}0\}$ overgrowth has progressed a lot further in these regions.

The overgrowth of the $\{10\bar{1}0\}$ facet does however never seem to complete even after extended growth times, but a small facet remain. This can be seen in fig. 6.11c and 6.11d, where a $\{11\bar{2}0\}$ facet is bordered by a $\{10\bar{1}0\}$ facet on the right hand side. That this is at a late stage in the overgrowth can be deduced due to the uncharacteristic morphology of the $\{11\bar{2}0\}$, i.e. no fingers. The type of morphology seen instead of the fingers has previously been observed during parallel experiments on InAs wires with severely overgrown $\{11\bar{2}0\}$ facets suggesting that this is the lower WZ segment (region VI).

The uncompleted overgrowth can at least partially be explained if the $\{10\bar{1}0\}$ facets grow radially in parallel to the $\{11\bar{2}0\}$ overgrowth. This type of growth is illustrated in fig. 6.9.

Regarding the interface between a WZ and a ZB segment, such transitions were generally found to be relatively placid, as can be seen in fig. 6.10. Atomically resolved STM images of such transitions, also provided in fig. 6.10, conveyed atomically sharp interfaces with possible stacking faults in the WZ crystal in close relation to the interface. No high resolution images regarding interfaces between the WZ$\{10\bar{1}0\}$ and WZ$\{11\bar{2}0\}$ facets were captured. In contrast to the WZ/ZB interface of fig. 6.6, which exhibits a rotation from the $\{110\}$ plane of the ZB into the $\{10\bar{1}0\}$ plane of the WZ crystal, analogous interfaces that had experienced extended overgrowth did not display any rotations. The reason for this is that in those cases $\{11\bar{2}0\}$ facet would have grown wide enough to cover the whole interface, as seen in fig. 6.10.

In summary the wire consists of 6 different segments, being alternating WZ and ZB crystals, separated by atomically sharp interfaces. The ZB segments exhibited the original $\{111\}$A and $\{111\}$B facets as well as zig-zag $\{110\}$ facets due to overgrowth. The width of the $\{110\}$ facet was much dependent on the exposure to growth conditions of the corresponding ZB segment, resulting in a very thin $\{110\}$ facet for region I, and an almost complete overgrowth for region V. The lower ZB segment, region V, would thus not exhibit any remnants of the underlying TSL structure, except a periodic 70°rotation of the $\{110\}$ atomic rows, and would have a truly hexagonal crossection with all facets being $\{110\}$ terminated.

The WZ segments, originally consisting of 6 $\{10\bar{1}0\}$ facets, exhibited $\{11\bar{2}0\}$ facets as a result of overgrowth. The overgrowth was however never completed and a consequential

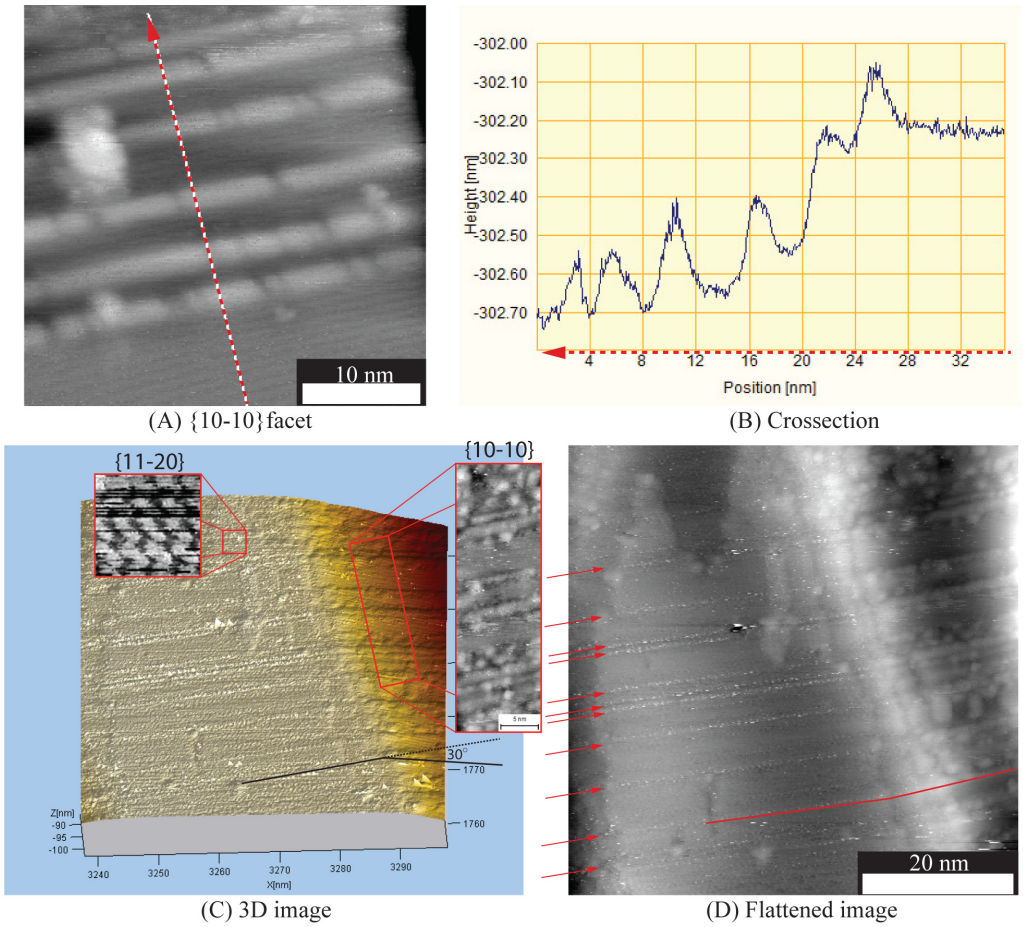

FIGURE 6.11. Figure (A) displayes a section of a $\{10\bar{1}0\}$ facet with visible atomic rows and sausages perpendicular to the growth direction (marked by arrow). The arrow in the figure also indicates the location of the line profile seen in figure (B). From the profile, it is clear that not all sausages are correlated to atomic steps. Figure (C) displays a 3D representation of the STM image seen in figure (D), depicting a part of WZ segment. Atomically resolved images of the top facet, revealing it as a $\{11\bar{2}0\}$ facet (inset figure), were necessary in order to determine the facet type since it did not exhibit any characteristic behavior of any of the facet types previously seen. Previous experiments done on InAs wires have however shown such morphology as a result of severe overgrowth, suggesting that this section of the wire would correspond to a WZ segment from either region IV or IV. The morphology of the right facet, as well as the angle between them being 30°, reveals it as a $\{10\bar{1}0\}$ facet. An additional feature of this image is that stacking faults can be seen, marked with red arrows in figure (B). Interestingly, the stacking faults seen on the $\{11\bar{2}0\}$ facet seem to correlate with the sausage positions of the $\{10\bar{1}0\}$ facet. This could explain why not all sausages could be correlated to atomic steps, since stacking faults could be as energetically favorable for nucleation as a surface step.

structure with 12 facets, 6 $\{10\bar{1}0\}$ and 6 being $\{11\bar{2}0\}$, could be found in these regions. The $\{11\bar{2}0\}$ facets appear to nucleate at the WZ/ZB interface and extend along the WZ segment from there. In the case of region II, the $\{11\bar{2}0\}$ growths from the two interfaces were not believed to reach each other, resulting in a section in the middle of the segment were the original 6 faceted $\{10\bar{1}0\}$ should be observed.

The lower located WZ segments, IV and VI, were however observed to have an overgrowth which had progressed a lot further, and the $\{11\bar{2}0\}$ facets from corresponding WZ/ZB interfaces did indeed reach each other, creating a single large $\{11\bar{2}0\}$ facet extending along the whole WZ segment. Although the $\{11\bar{2}0\}$ overgrowth had progressed further the $\{10\bar{1}0\}$ facets had not been completely overgrown, leaving thin $\{10\bar{1}0\}$ facets adjacent to the $\{11\bar{2}0\}$ growth.

2.3. Surface morphology. As previously discussed, the morphology of each facet had very distinctive characteristics, simplifying the process of identification. The individualities of those facets, in addition to the implications they convey, will be discussed in the sections below.

The WZ$\{10\bar{1}0\}$ facet was for instance found to exhibit numerous micro facets, with lengths ranging of 10-20 nm, separated by strings of adsorbents perpendicular to the growth direction. These lines, referred to as *sausages*, were often but not always correlated to atomic steps, as seen in fig. 6.11a and 6.11b.

The remaining images of fig. 6.11, (C) and (D), depict a highly overgrown $\{11\bar{2}0\}$ facet adjacent by a $\{10\bar{1}0\}$ facet. When seen from this larger perspective, it is clear that the number of micro facets and sausages are quite numerous, and in fact the abbundancy of those is unusally high in the mentioned image compared to other images of the facet in question.

An additional feature of interest regarding fig. 6.11c and 6.11d is that stacking faults are visible as slightly brighter atomic rows on the $\{11\bar{2}0\}$ facet. In fig. 6.11d these are marked out by red arrows. The fact that atoms related to a stacking fault can be observed in this fashion is correlated to change in the LDOS of such atoms, in analogy to step and edge atoms. This phenomenon can clearly be seen in fig. 6.10b.

Surprisingly, the stacking faults of the $\{11\bar{2}0\}$ appear to correlate with sausages of the adjacent $\{10\bar{1}0\}$ facet, as illustrated by the red line in fig. 6.11d. This poses an explanation to why not all sausages could be correlated to atomic steps, as is demonstrated in fig. 6.11a and the related crossection in fig. 6.11b. Although steps might be a favorable site for adsorption, stacking faults could possibly be equally favorable sites. Hence, deeming from these images, unless a sausage is located at a step it is most probably related to a stacking fault in the WZ crystal.

Additional findings regarding stacking faults were found on the $\{11\bar{2}0\}$ facets. It appears as if the characteristic finger growth of these facets originally start at the ZB/WZ interface as seen in fig. 6.10a. However, as seen in fig. 6.12, additional fingers often start or end in a stacking fault, marked out by the red lines. In addition, if a finger is not terminated at a stacking fault, but stretches on; the width of that finger will be altered when passing the stacking fault, as can clearly be seen in fig. 6.12c.

Another feature of the fingers of the lower $\{11\bar{2}0\}$ facet, i.e. region IV and VI, is that they generally were not found in the middle of a WZ segment, in between two ZB segments.

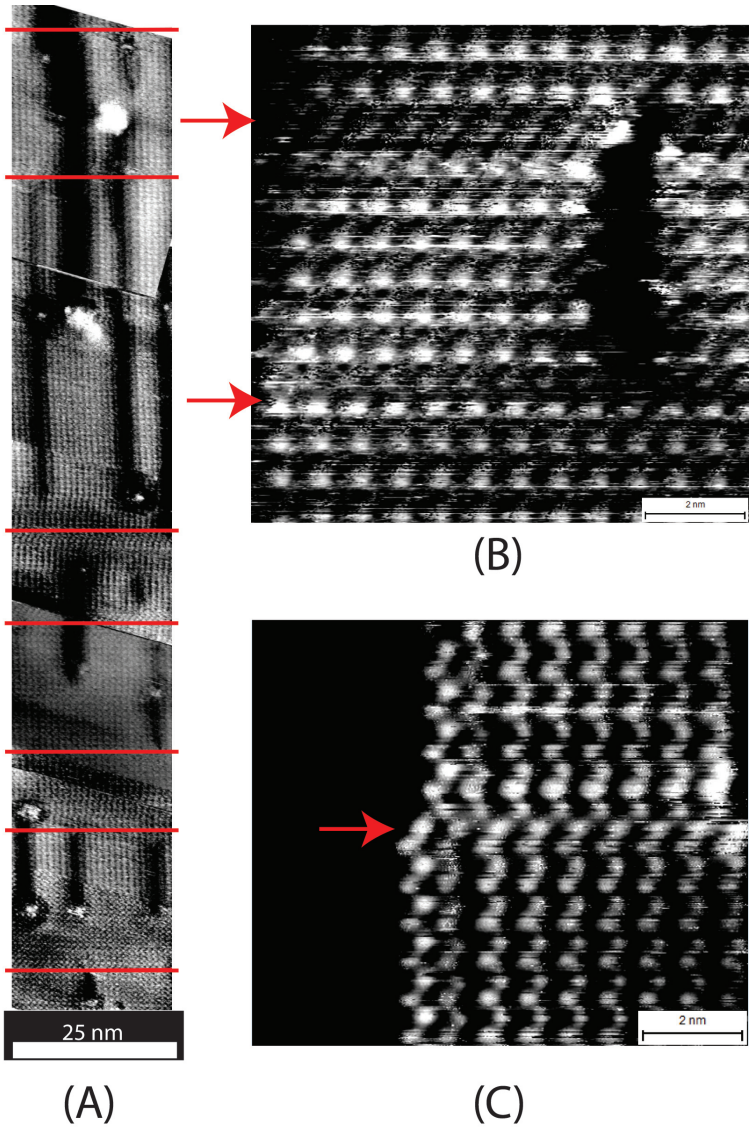

FIGURE 6.12. The figures depicts the $\{11\bar{2}0\}$ surface of a nanowire, and illustrates the density of stacking faults in the crystal, marked by red lines (A) or arrows (C and D). Figure (A) is a composite STM image extending along the nanowire direction. A clear correlation between stacking faults and finger growth/termination can be seen. This is shown in greater detail in figure (B). Figure (C) illustrates that the stacking faults will also cause the fingers to get thinner by one atomic row when passing a stacking fault. This makes it easy to identify stacking faults even though no atomic resolution is obtained.

As can be seen in fig. 6.7, they extend out from the ZB/WZ interface, believed to be the original nucleation site of the $\{11\bar{2}0\}$ facet and hence also the fingers, and then spread along the wire. A possible explanation for the absence of fingers in the middle of the WZ segment can be deduced by assuming that this will happen on the other ZB/WZ interface as well.

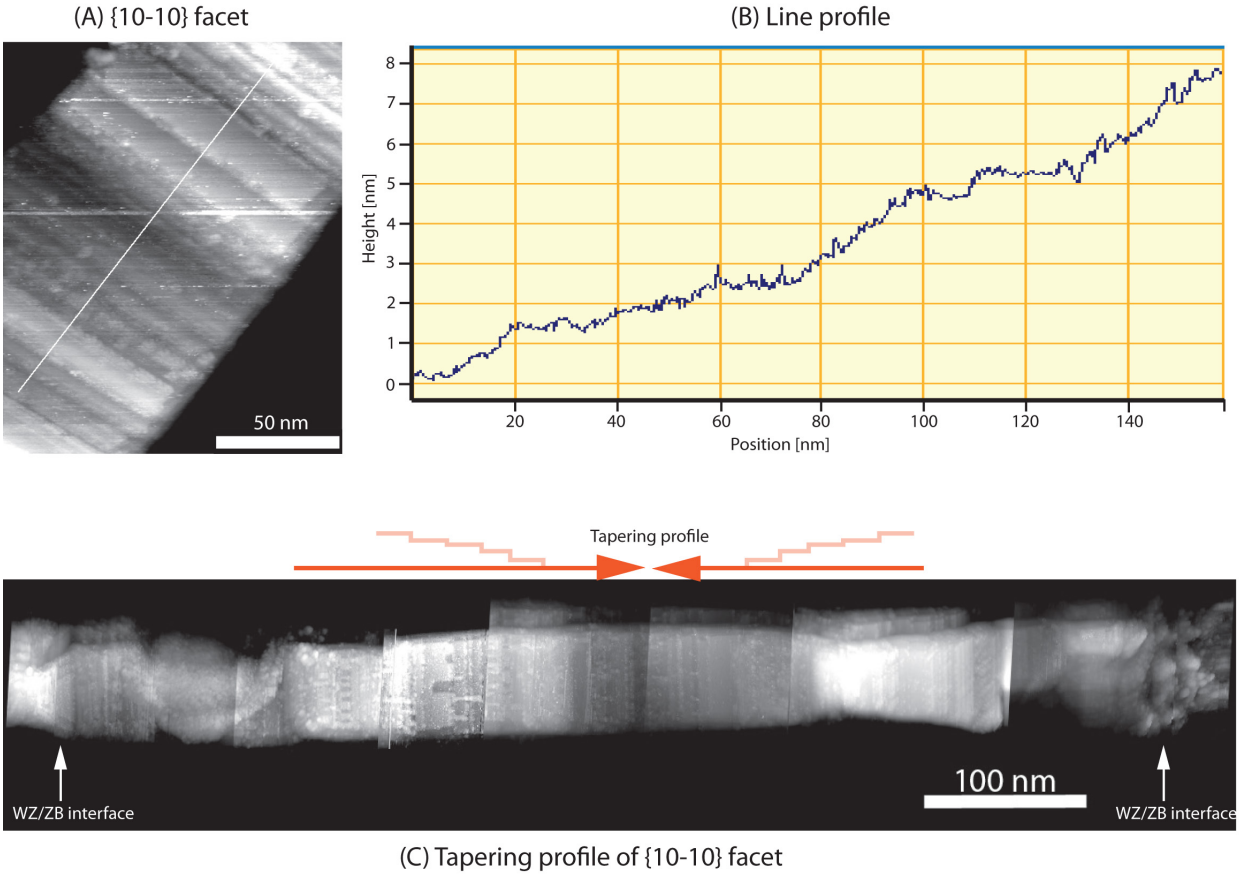

FIGURE 6.13. Figure (A) depicts portions of a $\{10\bar{1}0\}$ facet in the close vicinity of a WZ/ZB interface. The line profile of figure (B), defined by the white line in figure (A), reveals that the surface is highly tapered, approximately 5 nm tapering per 100 nm length along the wire. Figure (C) depicts a composite STM image of a $\{10\bar{1}0\}$ facet, with WZ/ZB interfaces at both ends, marked with white arrows. The red arrows illustrates the direction of the tapering, which suggests that the growth of the $\{10\bar{1}0\}$ facet starts at the WZ/ZB interfaces.

The fingers would then meet in the middle of the WZ segment and probably form a layer free of finger growth.

The fact that such fingers are observed at all suggests that once a nucleation site is found, axial growth from such a site is preferred over radial growth. This is also implied in the previously mentioned image from fig. 6.6, in which the $\{11\bar{2}0\}$ facet is very thin, but appears to extend quite far into the WZ segment. Hence, the diffusion length along the nanowire direction is a lot larger than in the direction perpendicular to the wire for the $\{11\bar{2}0\}$ surface. This is further supported by the fact that very few atomic steps are found on the $\{11\bar{2}0\}$ facets in general.

This is in great contrast to the $\{10\bar{1}0\}$ facet which exhibit a lot of steps, resulting in a high degree of tapering, as can be seen in fig. 6.13c. The figure depicts a $\{10\bar{1}0\}$ facet

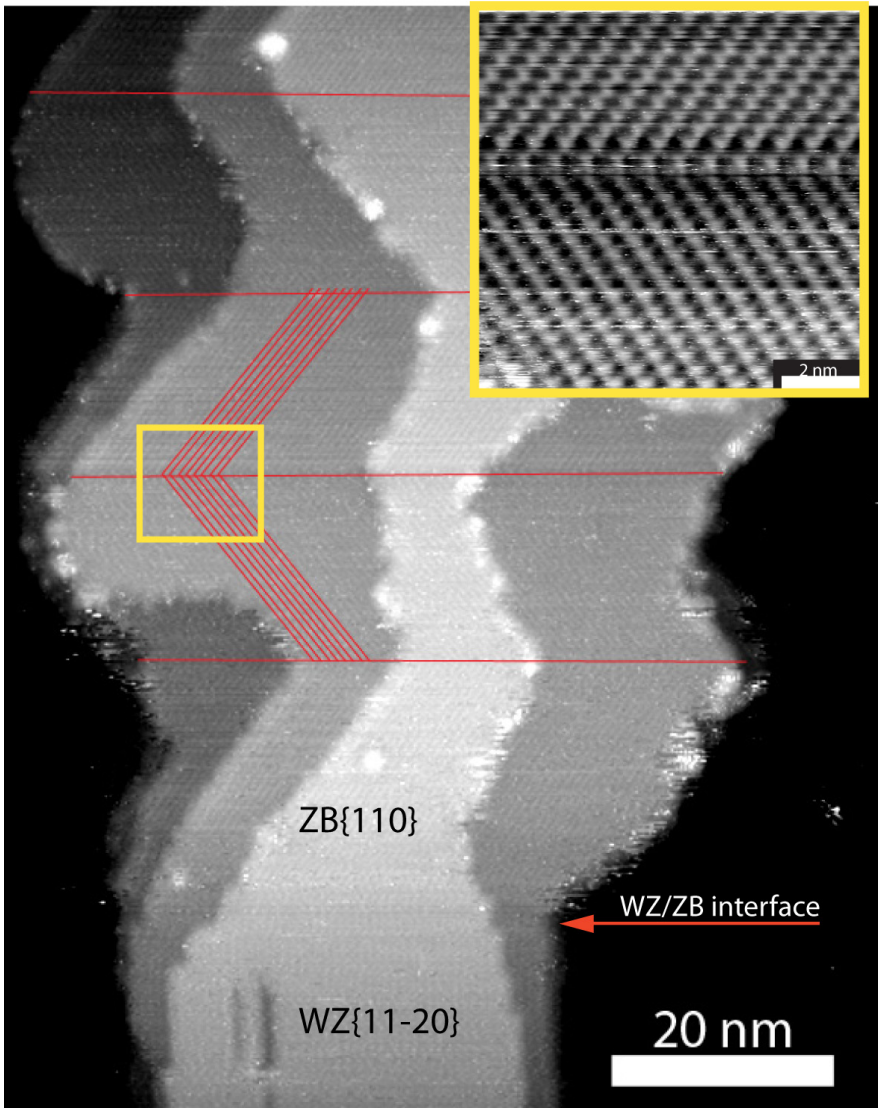

FIGURE 6.14. The figure depicts a ZB{110} surface, with the periodic mirror planes of the atomic rows marked out by red lines. As can be seen, the periodicity of the mirroring is 20-30 nm, which is in good correlation to the periodicity of the underlying TSL structure. The inset figure, marked by the yellow square, depicts the interface between two mirrored planes in greater detail. As can be seen, the atomic rows are rotated by a 70°angle with respect to each other, i.e. both having a 35°angle with respect to the growth direction.

from region II, and the direction of the steps are indicated by the arrows. By studying the tapering profile it becomes quite obvious that also the $\{10\bar{1}0\}$ prefers to grow from the WZ/ZB interface since a lot of steps are found in the vicinity of those. This is further illustrated in fig. 6.13b in which a line profile along a section of a $\{10\bar{1}0\}$ facet in close relation to a WZ/ZB interface can be seen.

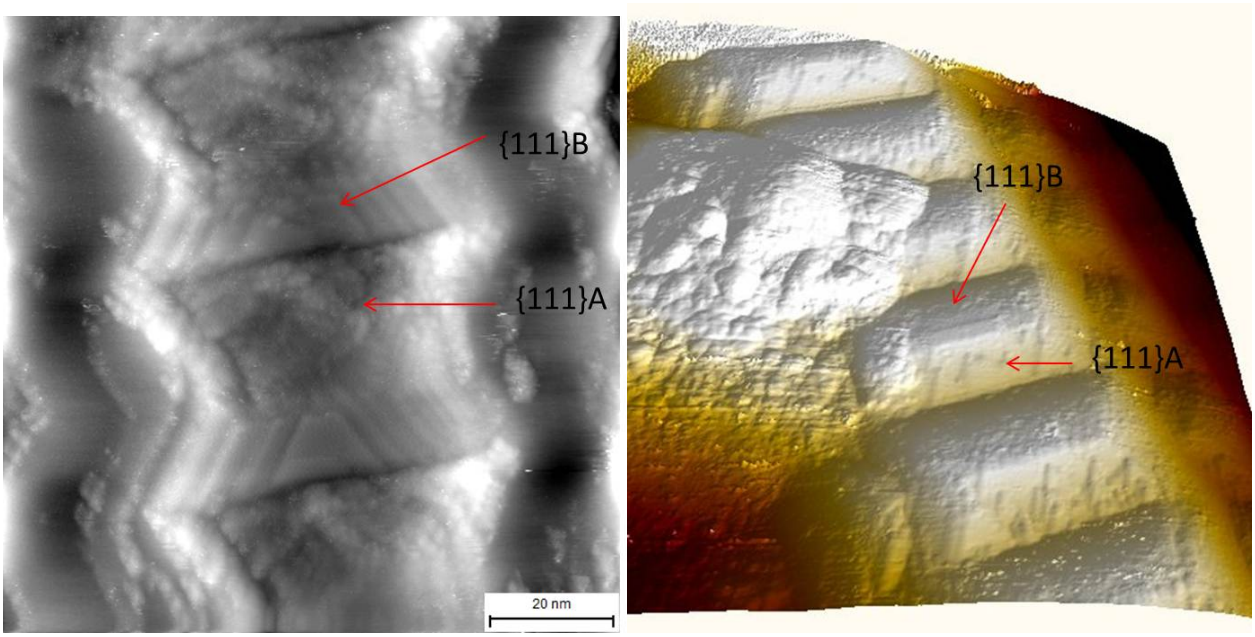

(A) STM image of TSL

(B) Larger scale 3D representation of STM image

FIGURE 6.15. An STM image (A) as well as a 3D representation of an STM image (B) depicting the {111}A and {111}B facets of the TSL structure. The big blob in the upper left part of figure (B) is fragments of the probing tip which was unintentionally dropped. As can be seen in both figures, the B surface appears to be clean and crystalline, whereas the A facet is rougher. In figure (B) a hint of a triangular structure can be seen on the A facet.

In addition it also indicates that the axial diffusion length of mobile adatoms is significantly lower as compared to the $\{11\bar{2}0\}$ surface. As a result if this, the $\{10\bar{1}0\}$ facet in fig. 6.13c should have a slightly bowl shaped profile, since a lot of growth will have occurred at the interfaces that have not been able to extend throughout the whole segment due to the low diffusion length.

Hence, instead of fingers, the $\{10\bar{1}0\}$ will form micro facets. A possible explanation of the sausages could be related to the finding regarding the fingers of the $\{11\bar{2}0\}$ facets and their preference to nucleate and terminate at stacking faults or interfaces. Once nucleation has started, axial growth from that spot seems to be preferred, resulting in the mentioned fingers. As the $\{11\bar{2}0\}$ facet is growing the whole stacking fault will soon be saturated. At the edges of the facet it is thus quite possible that some atoms might migrate over the edge onto the adjacent $\{10\bar{1}0\}$ facet. Since axial growth is not as preferred at this surface, the stacking fault would rather soon be saturated by a string of atoms, explaining the observed sausages at this surface. The same would apply for atomic steps on the $\{10\bar{1}0\}$ surface, which also exhibits sausages.

Although many stacking faults were found in the WZ parts of the wire, none were found on the ZB{110} facet. This can however be explained by the fact that a stacking fault in a

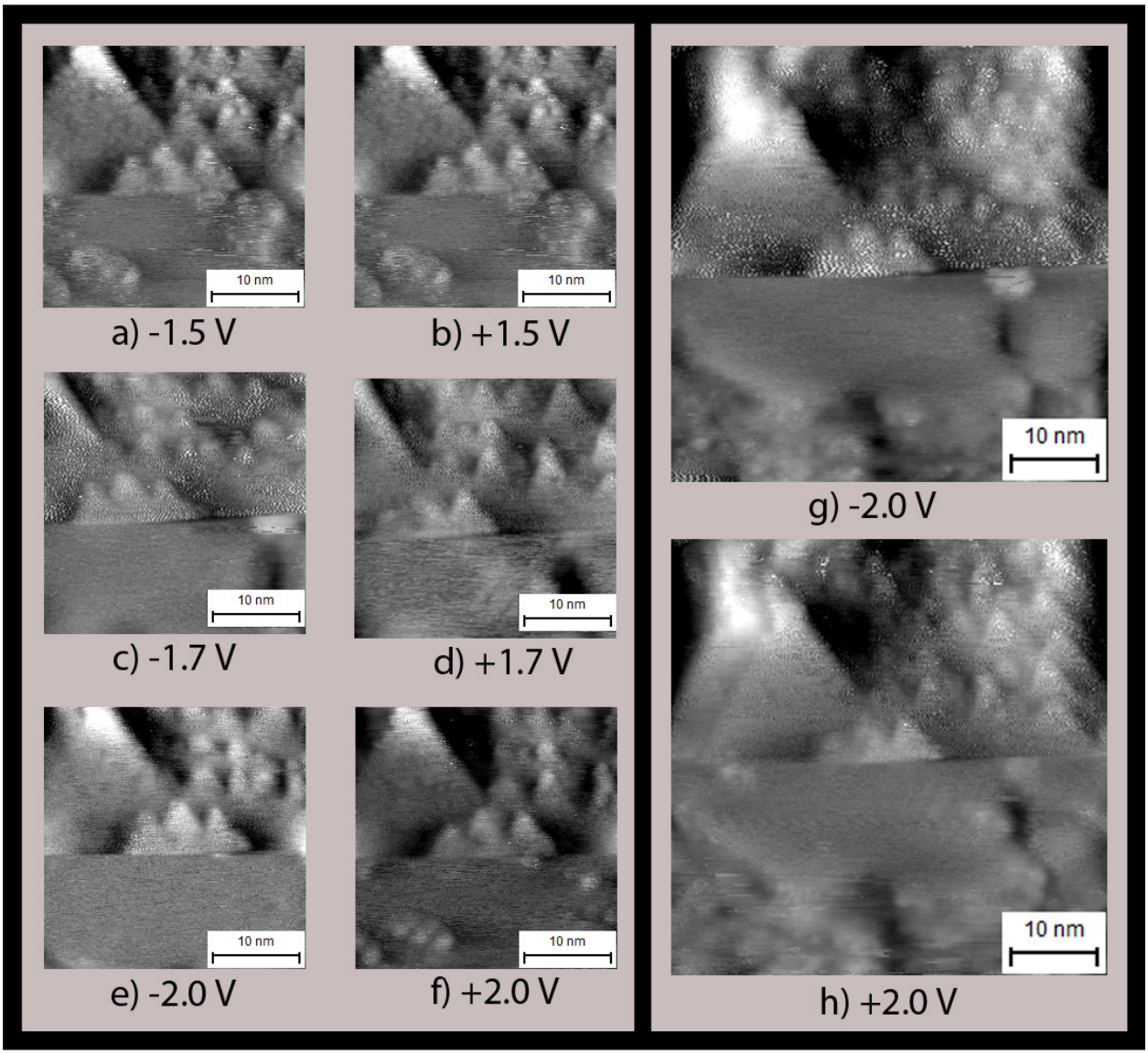

FIGURE 6.16. The same TPS segment, showing both the {111}A and {111}B facet, imaged at several different bias voltages. Images a)-f) have an image size of 30x30 nm, whereas g) and h) have an image size of 50x50 nm. A constant current of 80 pA was used in images g), h), c) and d), whereas a current of 150 pA was used for a), b), e) and f).

ZB crystal would shift the atomic rows one atomic step; hence a stacking fault would not be detected.

They only inconsistencies found in the atomic structure were the periodic shift of 70°in the direction of the atomic rows as depicted in fig. 6.14. The periodicity of the twin boundaries, 20-30 nm, matches that of the underlying TSL strongly suggesting that it is an inherent effect of that structure during the overgrowth. Although the twin boundaries could pose as preferable adsorption sites, much like the stacking faults of the WZ crystal, no observations

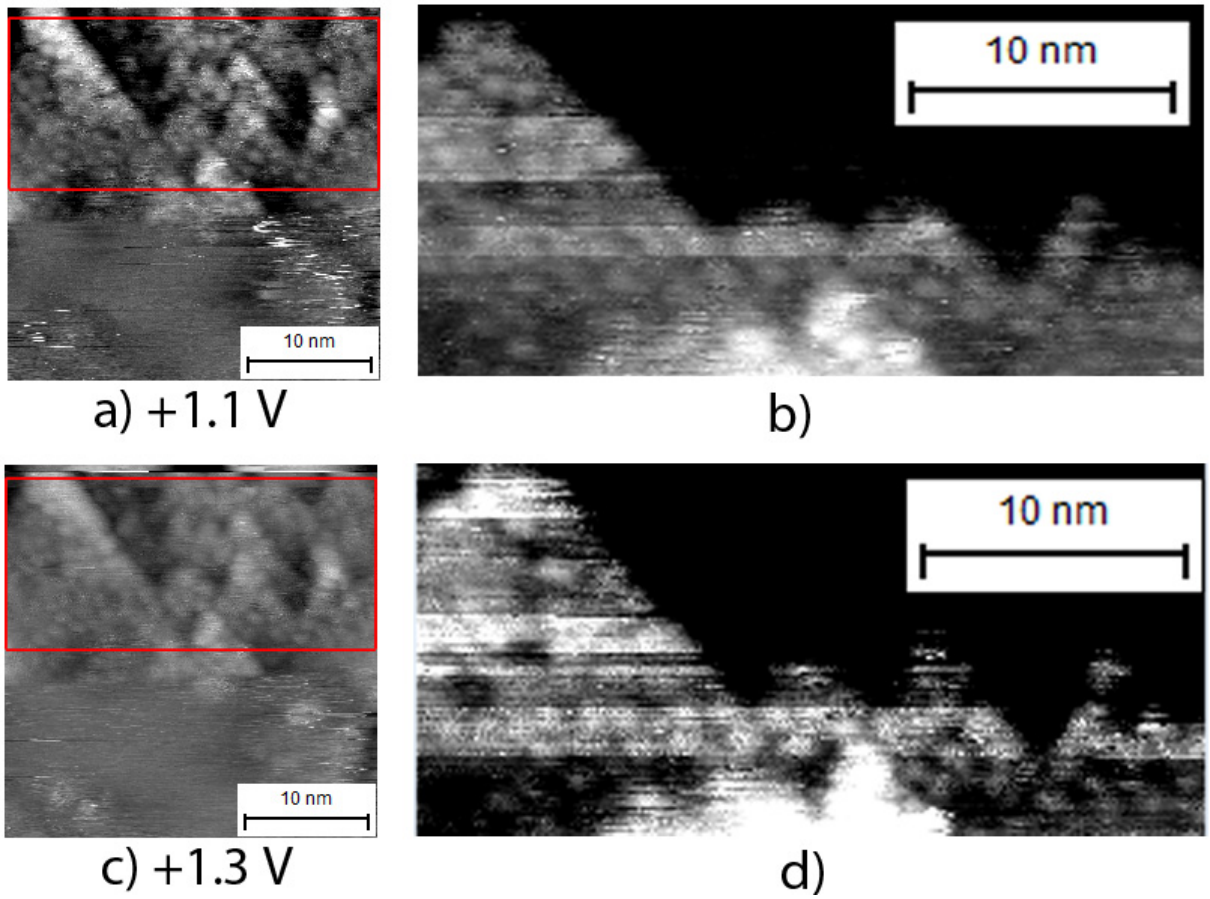

FIGURE 6.17. The {111}A facet of the TSL at two different voltages. In figure (b) and (d) the area marked by a red square in corresponding images can be seen in greater detail. A quasi periodic pattern of what appears to be atoms can be seen. The spacing between these atomic like structures is however too large, being approximately 2 nm, to correspond to the expected atomic lattice of a {111} facet. This suggests that the surface is reconstructed, possibly forming trimers.

of adsorbents were found on such sites. Hence, with the exception of the twin boundaries perpendicular to growth direction, this surface proved to be highly ordered on the atomic scale as can be seen in the inset figure marked by the yellow square in fig. 6.14.

Regarding the surface morphology of the facet, it was generally very flat with some irregular but large terraces as seen in fig. 6.14. These terraces usually stretched along the wire direction, rather then radially, suggesting that an axial growth is preferred on the ZB{110} facet. This is further supported by the fact that ZB{110} facets were found to stretch along the whole ZB segment of region I, see in fig. 6.5a, since a very fast axial overgrowth must have occurred for such a facet to form.

Additional findings regarding region I concern the {111}A and {111}B facets found in that region. As can be seen in fig. 6.15, the A and B exhibit very different surface

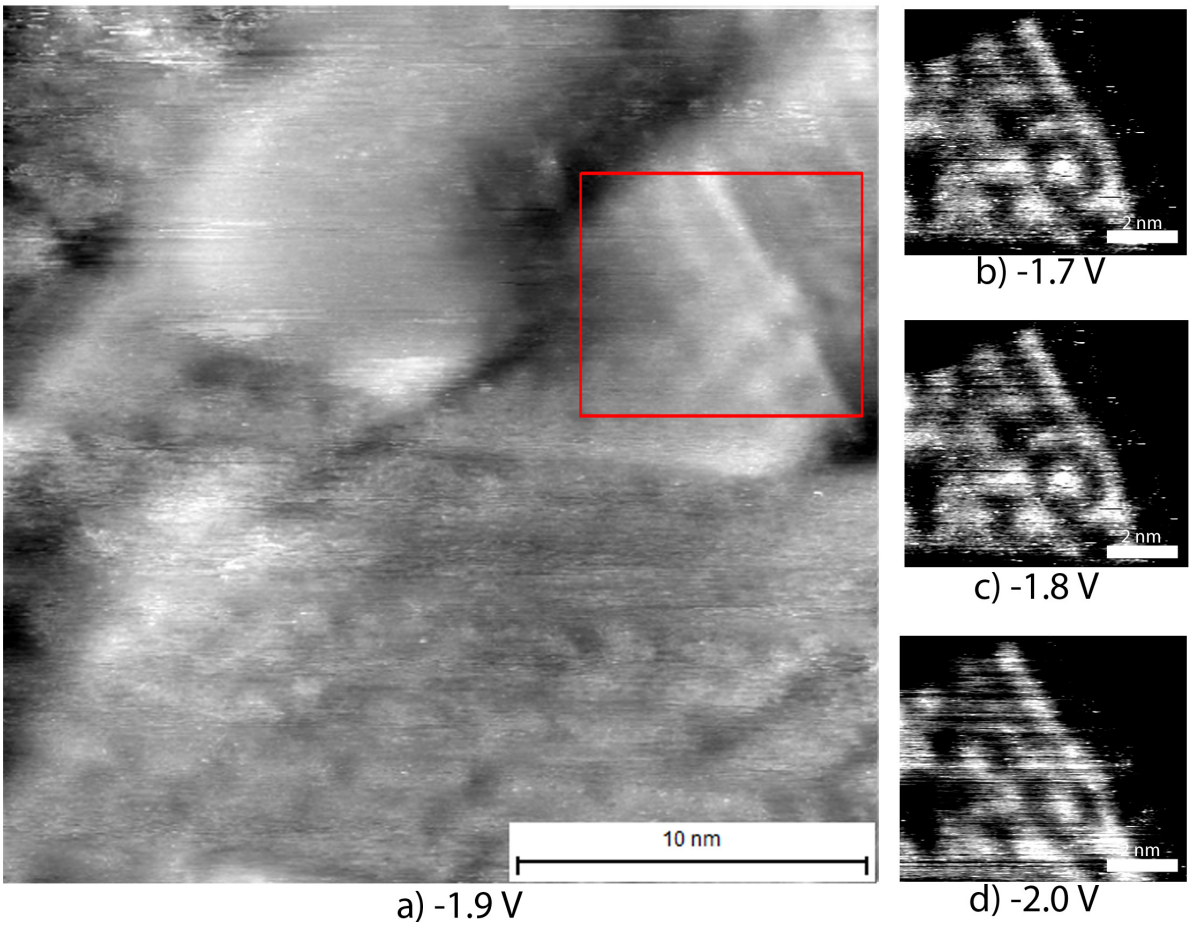

FIGURE 6.18. A small section of a {111}A facet, marked by the red square in figure (a), can be seen in greater detail and at different voltages in figure (b), (c) and (d). In the figures, a periodic assembly constructing a hexagonal pattern can be seen. Some of the atomic like structures exhibit a slight triangular shape and a relative distance corresponding to 2 nm between each other, further suggesting that they are trimers.

morphology. The B facet seems to be well ordered and flat, whereas the A facet appears to have a very irregular structure. This can at least partly be explained by previous findings regarding these surfaces in which they were found to overgrow at different rates [**9**].

Another explanation arises when considering that mostly negative tunneling voltages were used, probing mainly the filled states localized on the As atoms of a InAs surface. Since the A facet is terminated by In atoms, with a high local density of empty states, the surface could appear to be irregular and unstructured due to unstable tunneling between tip and sample due to the low density of empty states of those atoms.

When examined further and with a wider range of tunneling currents, including empty state imaging, i.e. positive voltage, a structure was indeed found also on the {111}A facet

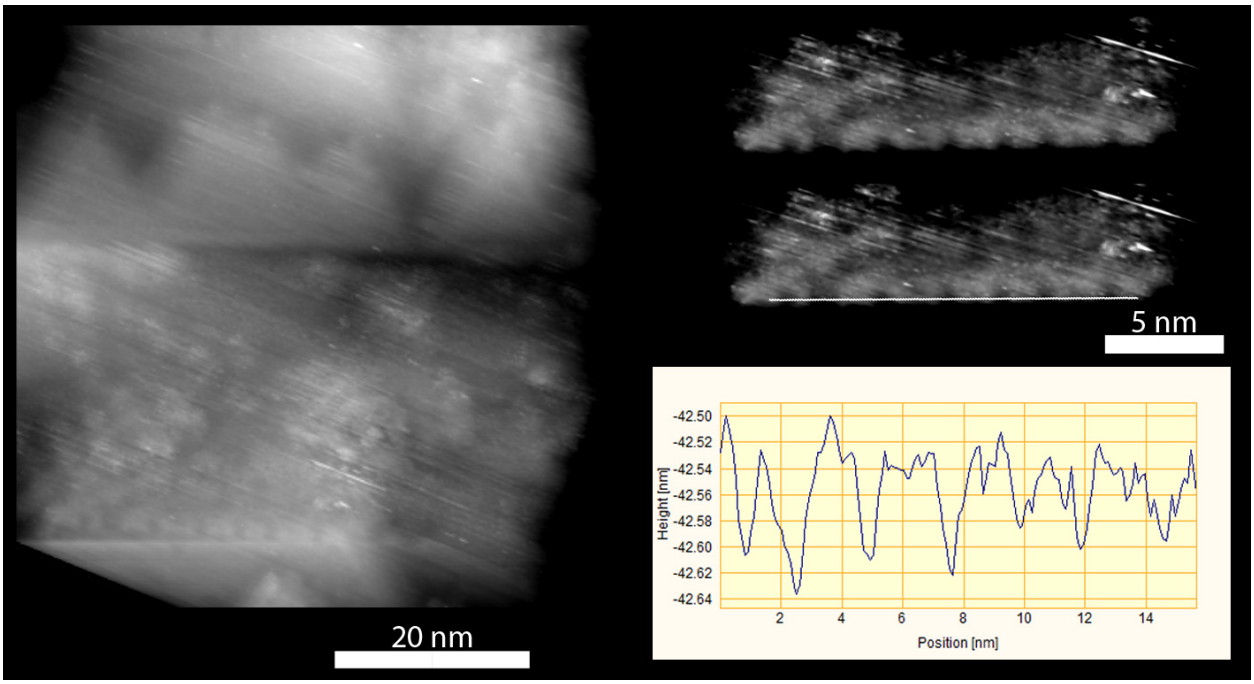

FIGURE 6.19. The figure illustrates that a well-spaced lattice, probably consisting of trimers, can be seen even at the top interface between the {111}A and {111}B facet of the TSL. The line profile of the interface, denoted by the white line, suggests that the relative position between the proposed trimers is approximately 2 nm.

as seen in fig. 6.16. As depicted in series of images of the figure, the surface morphology of the {111}A facet appears to consist of a number of triangular facets of varying sizes.

The image quality of the {111}A facet appears to improve when using positive voltages, consistent with the proposition of filled state imaging being the cause for this surface to look unstructured at large scale. As expected, the image quality of the {111}B facet decreases when utilizing empty state imaging, i.e. using a positive bias. Another trend for the {111}A facet appears to be that the tunneling is more stable, i.e. better image quality, at lower voltages, including lower negative voltages and even a hint of quasi periodic structure can be seen in fig. 6.16a and b. The {111}B facet appears to be unaffected by this. This fact can give a vague hint regarding the band structure of the respective surfaces. However, due to the lack of statistics, the possibility of these differences to be tip induced rather than a feature of the surfaces cannot be ruled out.

Regardless, the revealed triangular structure in addition to the semi periodic pattern found on the {111}A facet is still of interest. A more detailed representation of the facet can be seen in fig. 6.17, in which a couple of pictures are depicted, both utilizing empty state imaging. An enlarged version of the corresponding {111}A facet is depicted as fig. 6.17b and 6.17d in the figure. From these, the quasi periodic pattern can more clearly be seen, and it appears to have a somewhat hexagonal lattice, which would very well correspond to the expected atomic lattice found on such a facet. The periodicity, being in the range of approximately 2 nm, is however way to large to correspond to an atomic lattice.

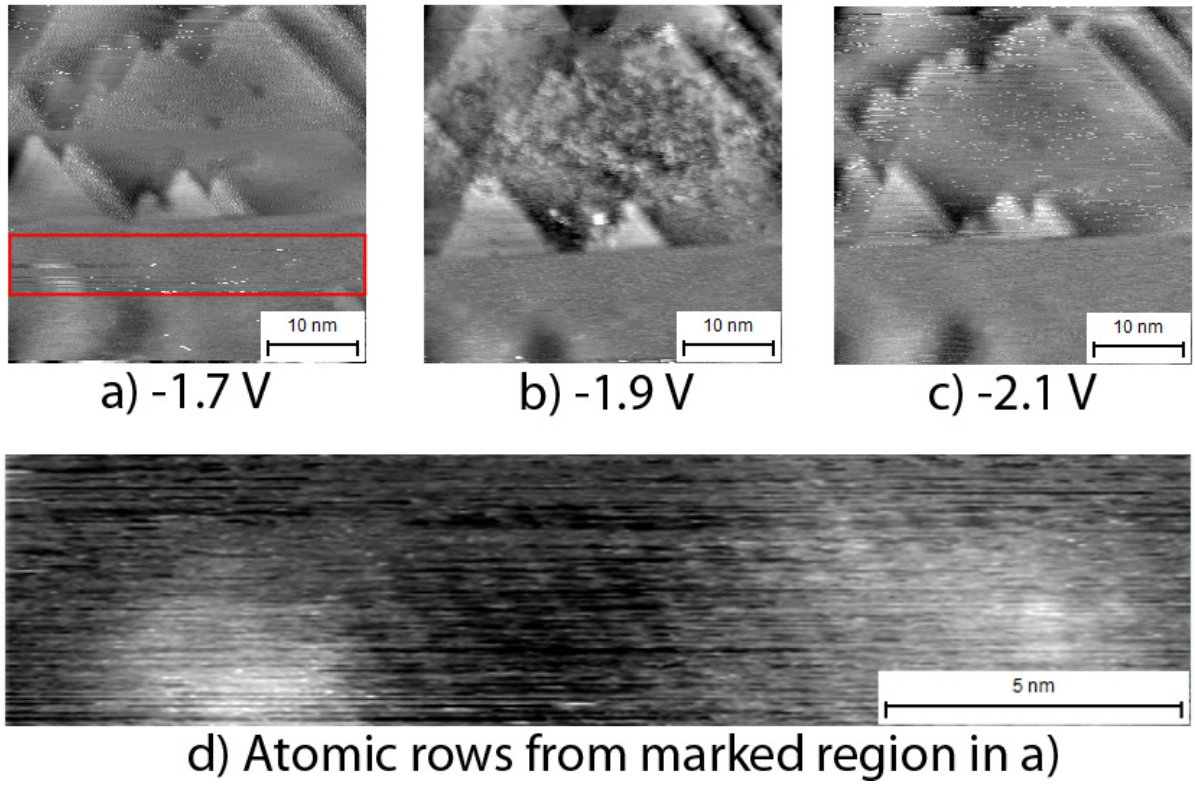

FIGURE 6.20. The figure depicts the {111}A/B interface at different voltages. As can be seen the quality of the A facet (upper) is highly dependent on the applied bias. This could be an effect of the suggested reconstruction of the surface, forming trimers. In figure (d), the {111}B facet, originally from the red square in figure (a), is shown in greater detail revealing weak atomic rows proving that the {111}B surface is not reconstructed.

In order to understand the origin of this structure additional images were taken on the surface, in even greater detail as depicted in fig. 6.18. The lattice structure seen in the figure is again found to have a periodicity of approximately 2 nm. Interestingly, the structure at such a small scale seems to be more ordered in comparison to the larger scale images from fig. 6.17, showing well-ordered rows related to a hexagonal lattice. In addition, parts of the atomic like structure exhibit a slight triangular shape, something which is common for trimers.

Thus it is possible that the atoms of the {111}A facet have formed trimers in a well ordered fashion. In such a case, the dangling bonds of 3 neighboring atoms will have bound together, forming a local density of states at a location in between the three. Such local density of states would then appear as an "atom" in an STM image, but with a lattice much greater than an atomic lattice, as have been observed.

Additional support for this theory was found when studying the peak interface between the {111}A and {111}B facet. As seen in fig. 6.19, a structure can be seen at the interface

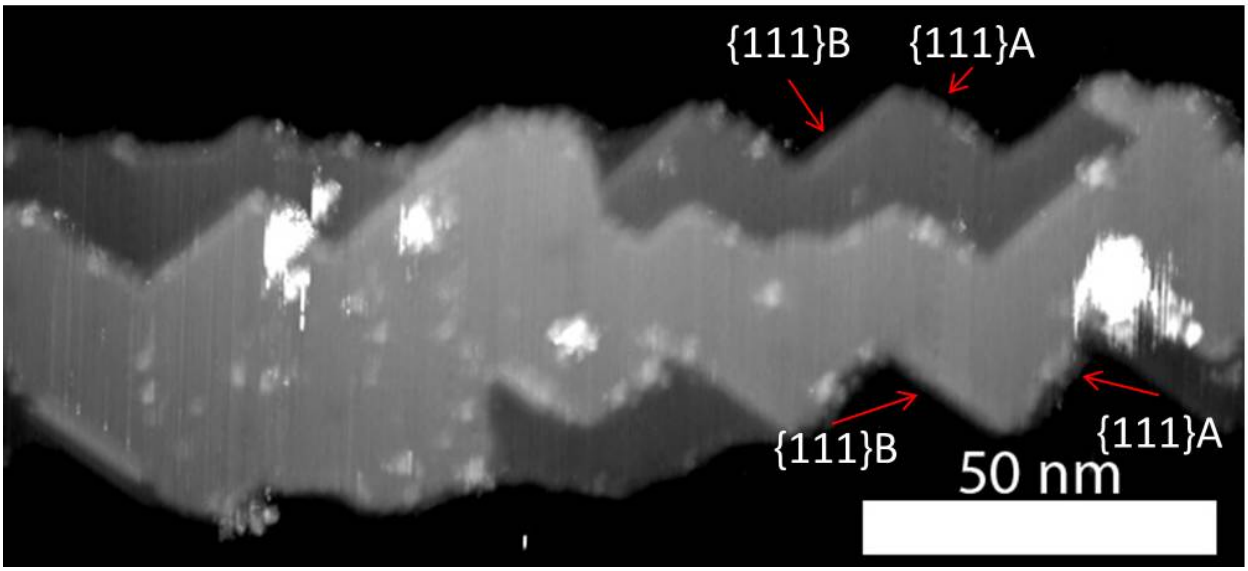

FIGURE 6.21. A ZB{110} facet. As pointed out by the arrows, the {111}A and {111}B facets (seen in profile) can be identified due to the fact that their surface morphology is different, being rougher for the A facet. Hence the A facet will look rough in profile, whereas the B facet will have nice straight lines. This makes it possible to determine the wire direction, only by studying the sawtooth edges of any {110} facet.

with a well-defined periodicity of roughly 2 nm. This implies that the suggested trimer formation stretches all the way to the interface.

The possibility of trimer formation on an InAs {111}A facet is feasible, and trimer associated reconstructions have previously been observed on bulk surfaces [**16**, **19**]. The mentioned study did however only concern an InAs {111}B surface, and the reconstruction was due to annealing with temperatures in the 600 ℃regime, something which have not been done in this study. No reconstruction was however found on the {111}B facet, as can be seen in fig. 6.20. If assuming that the annealing related to the cleaning procedure is the origin of the reconstruction, it would suggest that the {111}A surface is more sensitive to temperature related conditions. Although the trimer formation can be related to the cleaning procedures, a growth related cause cannot be ruled out.

The formation of trimers suggests that the dangling bonds of the original atomic structure are unsatisfied and energetically unfavorable. Such a surface would probably favor adsorption in order to satisfy the bonds, providing an explanation to why the {111}A surface appears to be overgrown in a higher rate when compared to the {111}B facet.

A higher growth rate of the {111}A is further implicated by the triangular structure found on the facet. When considering region I of the nanowire, the overgrowth of the {111} facets should not have transpired for too long, consistent with the flat surface found on the {111}B facet. The fact that triangles have formed on the {111}A facet at that stage in the growth, strongly suggests an accelerated overgrowth.

The overgrowth itself appears to start at the vale interface, as the triangles originate from there. The fact that several sizes of triangles, as well as several layers of them, can be seen suggests that the overgrowth does not occur in a layer by layer fashion.

It was found that the accelerated overgrowth of the {111}A facet could be used in order to determine the wire orientation only by studying any of the {110} facets, a fact that is of great value when trying to locate a specific region of the wire. For instance, by studying the {110} facet of fig. 6.21 it can clearly be seen that every other side of the sawtooth is sharper than the other.

Since the sawtooth edge can be considered as the {111}A/B facets in a 30°profile, the respective facets can be identified as done in the figure due to the sharpness relative to bulkiness, i.e. degree of overgrowth, of the sawtooth edges.

2.4. Electronic properties. The electronic properties of the nanowire surfaces were probed with STS, providing the $(dI/dV)/(\overline{I/V})$ spectra seen in fig. 6.22a. All facets were probed with the exception of the ZB{111}A/B facets of the TSL since no suitable tip quality for STS coincided with the imaging of the mentioned facet. Although not comparable to the analogous facets on the nanowire a reference spectrum of the {111}B InAs substrate is provided in fig. 6.22a, in order to ensure the tip quality. The measured spectrum was found to be in good correlation to previous STS studies on InAs(111)B substrates.

Regarding spectra related to the nanowire facets, the band gap width appears to be similar for all of them, being approximately 0.5 eV. This value, when considering slight band bending, is in good correlation with previous STS experiments on InAs surfaces suggesting bandgaps of 0.41-42 eV for general InAs surfaces, utilizing low temperature STS [**49**]. A bandgap of 0.36 eV for the bulk {110} plane was reported by Feenstra *et al.* in [**40**]. The position of the bandgap from their study also coincides with the recorded bandgap position of the {110} surface of the nanowire, suggesting that no surface effects perturbs the STS signal.

In addition, when comparing the atomically resolved images of the surface, fig. 6.2, with *density functional theory* (DFT) calculations assuming a non-reconstructed surface, a convincing correlation was seen [**8**]. This further suggests that no surface effects will have influenced the obtained spectra, and hence the electronic properties seen in the spectra can be compared to the bulk properties of the nanowire crystal.

The doping profile should be uniform throughout the whole wire since no doping gradient was used to achieve the variation in crystal structure. In addition, the spectra were obtained using the same tip which suggests that the band bending in the different spectra from the wire should be comparable. This does however not apply to the spectrum obtained at the substrate, explaining the large band gap as a result of severe band bending of spectrum. It is however possible to compare the band onset and offset between the spectra obtained on the nanowire.

As can be seen, a slight shift of the band gap position relative the Fermi level can be seen between the different facets. In addition, the shape of the conduction band seems to vary, as a linear increase of LDOS can be seen for the WZ$\{11\bar{2}0\}$ facet, whereas a polynomial increase can be seen for the WZ$\{10\bar{1}0\}$ facet and ZB{110} facet.

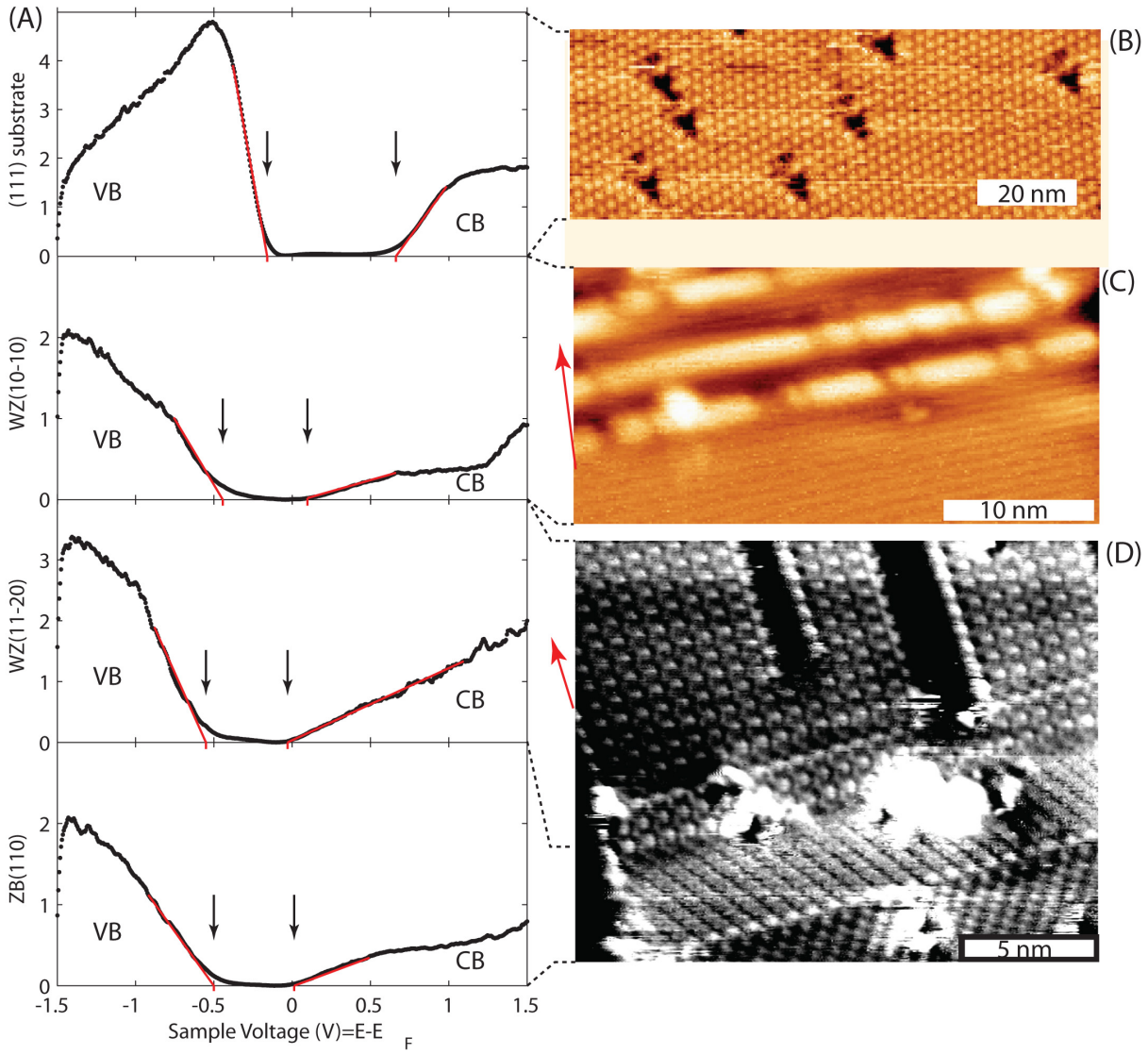

FIGURE 6.22. Figure (A) depicts spectroscopy data obtained from the given facets in the form of $(dI/dV)/(\overline{I/V})$ spectrum. The black arrows denote the band on sets and off sets. The red line indicates how these were estimated. Figure (B), (C) and (D) are sample images of the facets represented in the STS spectra from (A). (B) is the InAs(111)B substrate. Figure (C) is the WZ$\{10\bar{1}0\}$. Figure (D) depicts an interface between the WZ$\{11\bar{2}0\}$ (upper) and the ZB$\{110\}$ (lower). Approximately 10-15 spectra were averaged to obtain the curves depicted in (A).

CHAPTER 7

Summary

High resolution STM experiments were conducted on polytypic III-V nanowires exhibiting an axial stacking of periodic WZ and ZB segments. The resulting segments, originally exhibiting $\{10\bar{1}0\}$ facets for WZ and a TSL structure with $\{111\}$A/B facets for ZB, had experienced overgrowth based on the exposure to growth conditions. This gave rise to morphological differences, such as the formation of additional facets, between the originally analogous segments depending on their position along the wire. For instance, the WZ crystals were found to be overgrown by $\{11\bar{2}0\}$ facets which started nucleating at the WZ/ZB interface, and from there rapidly spreading axially along the wire. This overgrowth would occur at all WZ/ZB interfaces, and the growth at adjacent interfaces would thus meet in the middle of a WZ segment. The overgrowth was found to have progressed a lot further for the bottom WZ segments than for the uppermost, at which the overgrowth just had been initiated at the interface.

That the overgrowth is axially fast could be determined due to the observations of fingers along that direction of the wire, suggesting a high mobility of adatoms in the axial direction. In addition, even at the lower WZ segments, small $\{10\bar{1}0\}$ facets could still be found, being remnants of the underlying structure, suggesting that the radial overgrowth is not as effective as the axial.

Regarding the ZB TSL segments, a $\{110\}$ overgrowth was found, resulting in a flat facet with sawtooth edges, being a remnant of the underlying TSL structure. At the lower segments, the overgrowth had progressed significantly so that almost no TSL structure could be seen.

Due to the morphological differences between the different facets, such as abundance of steps, shapes of facet edges and other morphological landmarks such as fingers and sausages, the different facets could be identified without the need of atomically resolved images. That fact significantly reduces the search time for specific facets or interfaces.

Additionally, based on the morphological observations of the different facets, in diverse states of overgrowth, a suggested model of the nanowire structure could be created.

On the atomic scale, it was found that the ZB/WZ interfaces were atomically sharp, and well defined. However, a number of stacking faults could often be found in the close proximity of the interface in the WZ crystal. In fact, the WZ crystal in general exhibited quite a number of stacking faults, which are believed to be the nucleation sites for additional finger growth on the $\{11\bar{2}0\}$ surface. On the $\{10\bar{1}0\}$ surface, the stacking faults were found to be covered by a string of adatoms, denoted as sausages, with only a handful of very short fingers extending out from them. Hence suggesting that there is a difference regarding the apparent mobility of adatoms on the two facets.

Regarding the ZB TSL structure, the $\{111\}$A and $\{111\}$B facets were found to have been overgrown at different rates, with the B surface being nice and crystalline, while the A

facet where rougher. This could also be observed on the sawtooth edges overgrown {110} facet, with every other side of the sawtooth being flat and the other being rough. Hence the orientation of the nanowire could be determined by looking at any of the found ZB facets.

Additionally, the {111}A surface was found to be reconstructed, possibly having formed trimers. Why and how these trimers were formed is as of yet unknown, but a suggested possibility is related to exposure to high temperatures during the cleaning procedure. No reconstruction was found on the {111}B facet.

Regarding the STS experiments, it was concluded that no surface effects perturbed the obtained spectra, and the information obtained in those would correspond to the bulk properties of the nanowire. In addition, due to the homogeneous doping profile of the nanowire, the amount of band bending would be equal for all obtained spectra, suggesting that their band on and offsets could be compared. A small relative shift regarding those was found between the different facets in addition to different conduction band structure.

Outlook

The results presented in this study may not be revolutionizing in the sense that they directly would lead to a big leap forward in the electronic business. The fact that they were obtained at all is however, since the experimental barriers are high regarding STM on semiconducting nanowires, and as a result only a handful of papers have been published within the field.

The results do however provide a solid foundation for future studies related III-V nanowires, as a basic understanding of surface morphology and facet overgrowth is vital when taking nanowire devices to the next level. Additional impact is given by the fact that surfaces uniquely found in nanowire crystals such as the WZ crystal were studied, as it is the only way to characterize its surface morphology.

A next step would involve adding adsorbents to the nanowire surfaces since they have the potential to form quantum dots. This is of interest since tunable electronic properties is the ultimate goal of nanowires. Very little is however known about the effects of adsorbents on nanowires since an ample knowledge of the surface morphology and behavior is necessary prior to such experiments. Without it, there are simply too many parameters. Hopefully this, or similar, studies can provide such knowledge.

Another natural step would be to study similar polytypic wires constructed of other III-V materials, such as for instance GaAs or InP, in order to see if analogous morphology and overgrowth behavior is applicable in general for the related surfaces. Such knowledge could be of great use when regarding future fabrication of nanowires.

Such studies, regarding GaAs nanowires, were initiated but not completed during this study. However, some preliminary results, presented in fig. 7.1, suggest that there are differences related to the growth material when regarding the surface. The figure depicts a WZ/ZB interface between a $\{11\bar{2}0\}$ facet and a $\{110\}$ facet. In analogy to the InAs wires, the $\{11\bar{2}0\}$ facet exhibits the characteristic finger growth, stretching away from the interface. When studying the $\{110\}$ facet a number of vacancies can be observed, something which was not seen to that extent on the corresponding facet of the InAs wires. The fact that the no vacancies can be seen on the $\{11\bar{2}0\}$ facet suggests that the atomic bonds of that surface are stronger as compared to the $\{110\}$. Since a negative bias was used, it is most likely that the vacancies are due to missing As atoms.

Studying the $\{10\bar{1}0\}$, seen in fig. 7.2, it is apparent that no sausages can be observed, neither on the atomic steps or on any possible stacking faults. This suggests that the surface properties compared to the analogous facet on InAs wires are very different. In addition a higher abundance of fingers can be seen on this facet as compared to InAs $\{10\bar{1}0\}$ facets. It is however still highly tapered.

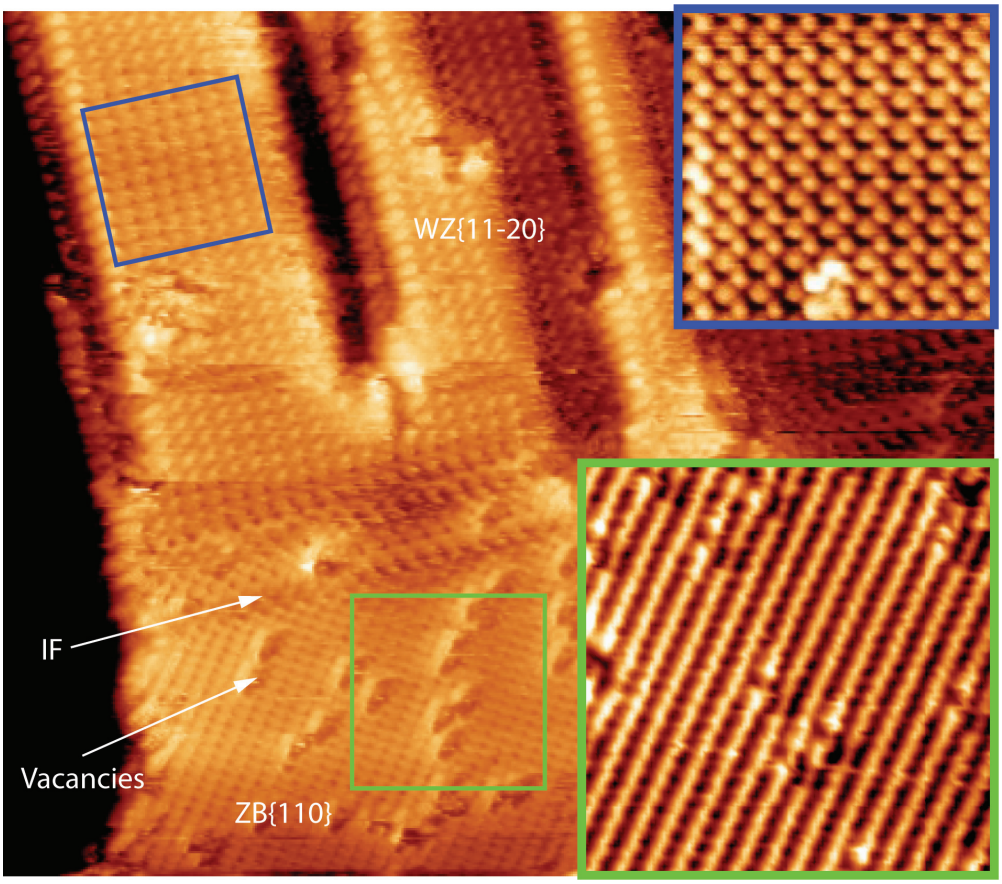

FIGURE 7.1. A WZ/ZB interface of a crystal engineered GaAs nanowire exhibiting both $\{11\bar{2}0\}$ facets and $\{110\}$ facets. In contrast to the $\{11\bar{2}0\}$ facet, the $\{110\}$ surface exhibit numerous vacancies in the atomic lattice. Such vacancies were not observed to such a degree on the analogous InAs surface. No abundance of vacancies on the $\{11\bar{2}0\}$ surface can be seen.

Since so many differences can be found when only briefly studying these GaAs nanowires, continuous studies would be of great interest if a more comprehensive understanding of nanowire surface morphology is to be achieved.

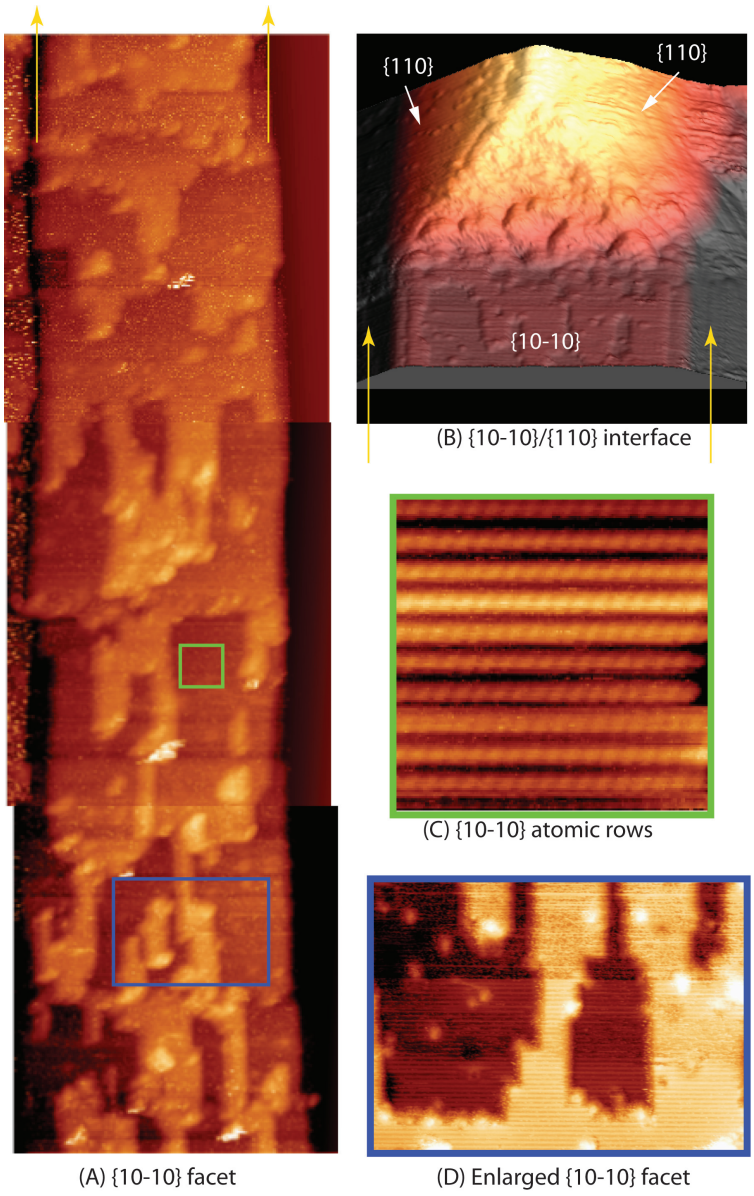

FIGURE 7.2. Figure (A) depicts a composite STM image of the $\{10\bar{1}0\}$ facet of a GaAs nanowire. In analogy to the InAs $\{10\bar{1}0\}$ facet, it is highly tapered. However, as can more clearly be seen in figure (D), no sausages can be observed either on the atomic steps or any possible stacking faults. In contrast to the analogous InAs surface, a higher abundance of finger growth can be observed. Figure (B) displays a transition from the $\{10\bar{1}0\}$ facet into two $\{110\}$ facets. A resulting high index facet is observed.

Bibliography

[1] J. Johansson, B. A. Wacaser, K. A. Dick, and W. Seifert, "Growth related aspects of epitaxial nanowires," *Nanotechnology*, vol. 17, no. 11, p. S355, 2006.

[2] M. W. Larsson, J. B. Wagner, M. Wallin, P. Håkansson, L. E. Fröberg, L. Samuelson, and L. R. Wallenberg, "Strain mapping in free-standing heterostructured wurtzite inas/inp nanowires," *Nanotechnology*, vol. 18, no. 1, p. 015504, 2007.

[3] C. M. Lieber, "Semiconductor nanowires: A platform for nanoscience and nanotechnology," *Materials Research Society*, vol. 36, pp. 1052–1063, 2011.

[4] E. D. Williams, "Nanoscale structures: Liability, length scales, and fluctuations," *MRS Bulletin*, 2004.

[5] H.-C. Jeong and E. D. Williams, "Steps on surfaces: Exeriment and theory," *Surface sience reports*, vol. 34, pp. 171–294, January 1999.

[6] P. Caroff, K. A. Dick, J. Johansson, M. E. Messing, K. Deppert, and L. Samuelson, "Controlled polytypic and twin-plane superlattices in iii-v nanowires," *Nature Nanotechnology*, vol. 4, no. 1, pp. 50–55, 2008.

[7] D. D. D. Ma, C. S. Lee, F. C. K. Au, S. Y. Tong, and S. T. Lee, "Small-diameter silicon nanowire surfaces," *Science*, vol. 299, no. 5614, pp. 1874–1877, 2003.

[8] E. Hilner, U. Hakanson, L. E. Froberg, M. Karlsson, P. Kratzer, E. Lundgren, L. Samuelson, and A. Mikkelsen, "Direct atomic scale imaging of iii-v nanowire surfaces," *Nano Letters*, vol. 8, no. 11, pp. 3978–3982, 2008. PMID: 18850752.

[9] T. Xu, K. A. Dick, S. Plissard, T. H. Nguyen, Y. Makoudi, M. Berthe, J.-P. Nys, X. Wallart, B. Grandidier, and P. Caroff, "Faceting, composition and crystal phase evolution in iiiv antimonide nanowire heterostructures revealed by combining microscopy techniques," *Nanotechnology*, vol. 23, no. 9, p. 095702, 2012.

[10] F. Glas, J.-C. Harmand, and G. Patriarche, "Why does wurtzite form in nanowires of iii-v zinc blende semiconductors?," *Phys. Rev. Lett.*, vol. 99, p. 146101, Oct 2007.

[11] R.M. and Feenstra, "A prospective: Quantitative scanning tunneling spectroscopy of semiconductor surfaces," *Surface Science*, vol. 603, no. 18, pp. 2841 – 2844, 2009.

[12] R. E. Algra, M. A. Verheijen, M. T. Borgstrom, L.-F. Feiner, G. Immink, W. J. P. van Enckevort, E. Vlieg, and E. P. A. M. Bakkers, "Twinning superlattices in indium phosphide nanowires," *Nature*, vol. 456, pp. 369–372, 2008.

[13] M. Hjort, *Surface studies of III-V nanowires*. PhD thesis, Lund University, 2012.

[14] B. Mandl, J. Stangl, T. Mårtensson, A. Mikkelsen, J. Eriksson, L. S. Karlsson, G. Bauer, L. Samuelson, and W. Seifert, "Au-free epitaxial growth of inas nanowires," *Nano Letters*, vol. 6, no. 8, pp. 1817–1821, 2006.

[15] C. dang, "Cristal densite surface." Website, 2009. [Online; accessed 2012-06-07].

[16] E. Hilner, *Characterization of Surfaces Relevant to Nanotechnology*. PhD thesis, Lund University, 2012.

[17] M. Hjort, "Direct imaging and electrical probing of nanowire surfaces," 2008.

[18] J. Johansson, L. S. Karlsson, C. P. T. Svensson, T. Mårtensson, B. A. Wacaser, K. Deppert, L. Samuelson, and W. Seifert, "Structural properties of (111)B -oriented IIIV nanowires," *Nature Materials*, vol. 5, pp. 574–580, 2006.

[19] E. Hilner, E. Lundgren, and A. Mikkelsen, "Surface structure and morphology of inas(111)b with/without gold nanoparticles annealed under arsenic or atomic hydrogen flux," *Surface Science*, vol. 604, no. 34, pp. 354 – 360, 2010.

[20] G.Binnig, H. Rohrer, C. Gerber, and E. Weibel, "Vacuum tunneling," *Physica*, vol. 109 & 110B, pp. 2075–2077, January 1983.

[21] G.Binnig, H. Rohrer, C. Gerber, and E. Weibel, "Tunneling through a controllable vacuum gap," *Applied Physics Letters*, vol. 40, pp. 178–180, January 1982.
[22] G.Binnig, H. Rohrer, C. Gerber, and E. Weibel, "Surface studies by scanning tunneling mcroscopy," *physical review Letters*, vol. 49, pp. 57–60, July 1982.
[23] G.Binnig and H. Rohrer, "Scanning tunneling microscopy," *Surface Science*, vol. 126, pp. 236–244, 1983.
[24] G.Binnig and H. Rohrer, "Surface imaging by scanning tunneling microscopy," *Ultramicroscopy*, vol. 11, pp. 157–160, 1983.
[25] G.Binnig and H. Rohrer, "Scanning tunneling microscopy on crystal surfaces," *Journal of Crystal Growth*, vol. 65, pp. 679–680, 1983.
[26] G. Binnig, H. Rohrer, F. Salvan, C. Gerber, and A. Baro, "Revisiting the 7x7 reconstruction of si(111)," *Surface Science Letters*, vol. 157, no. 2-3, pp. L373 – L378, 1985.
[27] G. Binnig, H. Rohrer, C. Gerber, and E. Weibel, "(111) facets as the origin of reconstructed au(110) surfaces," *Surface Science Letters*, vol. 131, no. 1, pp. L379 – L384, 1983.
[28] D. A. Bonnell, *Scanning probe microscopy and spectroscopy: theory, techniques, and applications*. 2001.
[29] J. Tersoff and D. R. Hamann, "Theory of the scanning tunneling microscope," *Phys. Rev. B*, vol. 31, pp. 805–813, Jan 1985.
[30] C. J. Chen, *Introduction to Scanning Tunneling Microscopy*. 2008.
[31] G. Tahmasebipour, Y. Hojjat, V. Ahmadi, and A. Abdullah, "Optimization of stm/fim nanotip aspect ratio based on the taguchi method," *The International Journal of Advanced Manufacturing Technology*, vol. 44, pp. 80–90, 2009. 10.1007/s00170-008-1799-4.
[32] Z. Yu, C. Wang, Y. Du, S. Thevuthasan, and I. Lyubinetsky, "Reproducible tip fabrication and cleaning for uhv stm," *Ultramicroscopy*, vol. 108, no. 9, pp. 873 – 877, 2008.
[33] I. Ekvall, E. Wahlstrom, D. Claesson, H. Olin, and E. Olsson, "Preparation and characterization of electrochemically etched W tips for STM," *MEASUREMENT SCIENCE & TECHNOLOGY*, vol. 10, pp. 11–18, JAN 1999.
[34] R. M and Feenstra, "Scanning tunneling spectroscopy," *Surface Science*, vol. 299300, no. 0, pp. 965 – 979, 1994.
[35] R. M. Feenstra, J. A. Stroscio, J. Tersoff, and A. P. Fein, "Atom-selective imaging of the gaas(110) surface," *Phys. Rev. Lett.*, vol. 58, pp. 1192–1195, Mar 1987.
[36] P. Ebert, "Defects in iiiv semiconductor surfaces," *Applied Physics A: Materials Science and Processing*, vol. 75, pp. 101–112, 2002. 10.1007/s003390101059.
[37] G. Binnig, H. Rohrer, C. Gerber, and E. Weibel, "7 $\times$ 7 reconstruction on si(111) resolved in real space," *Phys. Rev. Lett.*, vol. 50, pp. 120–123, Jan 1983.
[38] S. M. Sze, *Semiconductor Devices: Physics and Technology*. River Street, Hoboken: Wiley, 2001.
[39] P. Mårtensson and R. M. Feenstra, "Geometric and electronic structure of antimony on the gaas(110) surface studied by scanning tunneling microscopy," *Phys. Rev. B*, vol. 39, pp. 7744–7753, Apr 1989.
[40] R. M. Feenstra, "Tunneling spectroscopy of the (110) surface of direct-gap iii-v semiconductors," *Phys. Rev. B*, vol. 50, pp. 4561–4570, Aug 1994.
[41] C. . Shih, S. Gwo, A. Smith, K. Chao, G. Guttroff, and J. Ketro, "Scanning probe microscopy of semiconductor heterostructures," *Scanning Microscopy*, vol. 12, no. 1, pp. 43–59, 1998.
[42] R. M. Feenstra and J. A. Stroscio, "Tunneling spectroscopy of the gaas(110) surface," *Journal of Vacuum Science & Technology B: Microelectronics and Nanometer Structures*, vol. 5, no. 4, pp. 923–929, 1987.
[43] R. M. Feenstra, Y. Dong, M. P. Semtsiv, and W. T. Masselink, "Influence of tip-induced band bending on tunnelling spectra of semiconductor surfaces," *Nanotechnology*, vol. 18, no. 4, p. 044015, 2007.
[44] J. Goldstein, D. Newbury, D. Joy, C. Lyman, P. Echlin, E. Lifshin, L. Sawyer, and J. Michael, *Scanning electron microscopy and x-ray microanalysis*. a: Springer, 2003.
[45] M. M.H., D. K., M. J.-O., B. J.-O., and S. L., "Size-selected gold nanoparticles by aerosol technology," *Nanostructured Materials*, vol. 12, no. 1, pp. 45–48, 1999.
[46] R. S. Wagner and W. C. Ellis, "Vapor-liquid-solid mechanism of single crystal growth," *Applied Physics Letters*, vol. 4, no. 5, pp. 89–90, 1964.
[47] Y. Wu and P. Yang, "Direct observation of vapor-liquid-solid nanowire growth," *J. Am. Chem. Soc.*, vol. 123, no. 13, pp. 3165–3166, 2001.

[48] T. Mårtensson, J. B. Wagner, H. E., A. Mikkelsen, T. C., J. Stangl, B. Ohlsson, G. A., L. E., S. L., and S. W., "Epitaxial growth of indium arsenide nanowires on silicon using nucleation templates formed by self-assembled organic coatings," *Adv. Mater.*, vol. 19, p. 18011806, 2007.

[49] I. Vurgaftman, J. R. Meyer, and L. R. Ram-Mohan, "Band parameters for iii–v compound semiconductors and their alloys," *Journal of Applied Physics*, vol. 89, no. 11, pp. 5815–5875, 2001.